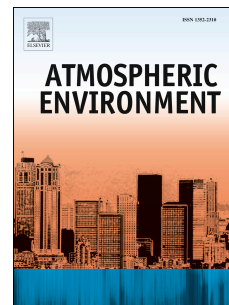


Journal Pre-proof

Revisiting the strong and weak ENSO teleconnection impacts using a high-resolution atmospheric model

Muhammad Mubashar Ahmad Dogar, Mansour Almazroui



PII: S1352-2310(21)00688-9

DOI: <https://doi.org/10.1016/j.atmosenv.2021.118866>

Reference: AEA 118866

To appear in: *Atmospheric Environment*

Received Date: 12 March 2021

Revised Date: 10 November 2021

Accepted Date: 21 November 2021

Please cite this article as: Ahmad Dogar, M.M., Almazroui, M., Revisiting the strong and weak ENSO teleconnection impacts using a high-resolution atmospheric model, *Atmospheric Environment* (2021), doi: <https://doi.org/10.1016/j.atmosenv.2021.118866>.

This is a PDF file of an article that has undergone enhancements after acceptance, such as the addition of a cover page and metadata, and formatting for readability, but it is not yet the definitive version of record. This version will undergo additional copyediting, typesetting and review before it is published in its final form, but we are providing this version to give early visibility of the article. Please note that, during the production process, errors may be discovered which could affect the content, and all legal disclaimers that apply to the journal pertain.

© 2021 Published by Elsevier Ltd.

D. M. M designed and performed the experiments, derived the models and analyzed the data. He wrote the complete manuscript. All authors contributed in final editing and revision of the manuscript.

Journal Pre-proof

1 **1. Introduction**

2 El Niño–Southern Oscillation (ENSO) is an interannual climate variability pattern that has
3 tremendous affects on the climate of the tropical and subtropical regions (Trenberth et al. 1998;
4 Timmermann et al. 1999; Neelin et al. 1998; Trenberth and Caron, 2000; Lee et al. 2010, 2012;
5 Zhang et al. 2011). The warming and cooling phases of this Pacific inter-annual variability are
6 termed as El Niño and La Niña respectively. Both these phases have worldwide climatic
7 interactions with important ecological and socioeconomic implications (Timmermann et al., 1999).

8 The physical link between ENSO variability and associated temperature, precipitation and wind
9 changes at the global and regional scale has been assessed in many studies (Timmermann et al.,
10 1999; Trenberth et al., 1998; Diaz et al., 2001; Ashok et al. 2001, 2004; Molteni et al., 2003; Bracco
11 et al., 2007, Kucharski et al., 2013; Kripalani et al., 2007; Dogar et al., 2019; Dogar and Shahid,
12 2019). Several past studies have shown a strong correlation between Eastern and Central Equatorial
13 Pacific sea surface temperature variability and rainfall pattern over the Pacific, Atlantic, Indian
14 Ocean and associated continental regions with focus on South Asia, Southeast Asia and Africa (Lee
15 et al., 2010; Kucharski et al. 2013; Zhang et al., 2011, 2012, 2013; Afzaal et al., 2013; Wang et al.
16 2012; Rasmusson and Carpenter, 1983]. ENSO is known to be the largest climatic forcing which
17 deals with variability of interannual monsoon system through the large-scale east-west displacement
18 of heat transfer in the tropics [Kumar et al. 1999a].

19 Many recent studies have shown that the American, Asian, Indian, and Australian rainfall systems
20 are greatly influenced by the ENSO teleconnection (Lau et al., 2000; Bracco et al., 2007; Lean et
21 al., 2008; Kripalani et al., 2007). Numerous studies have shown the simultaneous association of
22 ENSO-indices and the rainfall over India (Pant and Parthasarathy, 1987; Ashok et al. 2001, 2004;
23 Kripalani et al. 2007; Wu et al., 2012). Using observation and reanalysis products, Singh et al.
24 (2013) investigated the mechanisms and teleconnections behind the long-term variability in the
25 Indian Ocean SST, with a particular focus on SST in the southwestern Indian Ocean tropics. This
26 study concludes that boreal winter (DJF) SST is highly dependent on long-lived La Niña impacts,
27 indicating the importance of SSTs in the Indian Ocean, in addition to SSTs in the Pacific, to better
28 represent ENSO-induced teleconnections.

29 The original idea describing physical connection between ENSO forcing and South Asian monsoon
30 system, in particular the Indian monsoon, through large-scale dynamic circulation was initially
31 proposed by Gilbert Walker (Walker, 1925). Subsequently, several studies have shown that the
32 warm phase (El Niño) leads to the weakening of the Indian monsoon system with an overall
33 decrease in precipitation (Bhalme and Mooley, 1980; Rasmusson and Carpenter, 1983; Shukla and
34 Paolino, 1983; Ju and Slingo, 1995; Ashok et al. 2001, 2004; Dogar et al., 2017a). Conversely, the
35 cold phase (La Niña) is associated with an intensification of the Indian monsoon system and
36 increased precipitation [Shukla and Paolino 1983; Joo and Slingo, 1995). Many other studies have
37 also discussed the variations in the relationships between monsoonal rainfall and its predictors

1 (Parthasarathy et al., 1991a, 1992, 1994; Ashok et al. 2001). These variations are attributed to
2 change in ENSO characteristics such as period and amplitude (Kumar et al. 1999b).

3 Previous studies have shown that the ENSO, which originates in the central Pacific and in the east
4 Pacific, has significant variations and nonlinearities in its pattern, strength and associated climatic
5 impacts (Frauen et al., 2014; Chung et al., 2013; Hoerling et al., 1997; Wu et al., 2020; Wu and
6 Zhuoqi, 2019). However, it is difficult to distinguish weather these are caused by the different
7 signs/types, strengths, or spatial patterns of such events (e.g., strong or weak El Niño events or by
8 combinations of these).

9 In the past couple of decades, there has been an increase in both frequency and strength of
10 El Niño (La Niña) events with maximum warming (cooling) occurring in the central equatorial
11 Pacific (e.g., Latif et al., 1997; Afzaal et al., 2013; Lee et al., 2010). This is called as Central Pacific
12 (CP) El Niño (Yu and Kim, 2010; Kao and Yu, 2009), dateline El Niño (Larkin and Harrison,
13 2005), El Niño Modoki (Ashok et al., 2007) or warm pool El Niño (Kug et al. 2009). While
14 previous studies on ENSO events have discussed an increasing frequency of El Niño and La Niña
15 events in recent decades (Yeh et al. 2009; Lee et al. 2010; Timmermann et al., 1999), studies on the
16 magnitude and nonlinearity of El Niño and La Niña events are still evolving, and require further
17 research. Therefore, there is a need to look at the strength of ENSO variability and associated global
18 and regional climatic impacts. Being an important and leading mode of interannual climate
19 variability, El Niño Southern Oscillation produces significant impacts on global and regional
20 climate; hence there is a great interest in studying how the magnitude of the tropical Pacific sea
21 surface temperature would affect tropical global climate patterns (including large scale circulations)
22 and related changes in temperature and precipitation distribution.

23 Although the existence of the Hadley cell and its sensitivity to ENSO episodes has been
24 extensively investigated (Held and Hou 1980; Seager et al. 2003; Feng and Li, 2013; Nguyen et al.,
25 2013), questions remain, as to how this thermally driven large-scale tropical Hadley circulation will
26 respond to ENSO strength (i.e., strong and weak ENSO). For this purpose, we will make use of a
27 high-resolution atmospheric model, HiRAM with a resolution that generally is used by regional
28 climate models in climate downscaling studies for better representation of regional climate
29 processes influenced by global scale patterns. The HiRAM has effectively been used to study global
30 and regional climatic changes (Bangalath et al., 2015; Dogar et al., 2017b; Dogar, 2018; Dogar and
31 Shahid, 2018; Dogar, 2020). In this study, we will see how well it can reproduce the impact of
32 strong and weak ENSO events at the global and regional scale. The use of high-resolution modeling
33 technique provides us a unique opportunity to examine how the ENSO-induced circulation
34 anomalies at various scales influence regional climate. To the best of our knowledge, there is rarely
35 any study pertaining to regional ENSO impacts using a Global Climate Model (GCM) at a spatial
36 resolution of about 25 km or better; hence, in this sense this study is very useful for its successors.
37 Besides, this version of HIRAM is effective in overcoming many of the limitations encountered by

1 coarse-resolution GCMs and RCMs. Due to their fine grid spacing, important processes such as
2 large-scale condensation, land-sea interaction, and topographical forcing are better resolved in high-
3 resolution GCMs (Boyle & Klein, 2010; Lau & Ploshay, 2009; Harris et al., 2016). Recent studies
4 further emphasized that the regional convective structure and precipitation change are very sensitive
5 to the model horizontal resolution (Bui et al., 2019; Liu, Yu, & Chen, 2018). The idea of conducting
6 HIRAM AMIP simulations is to see if there could be any improvement in the simulations of ENSO
7 response especially at regional scale with improved resolution.

8 As Hadley circulation transport energy from equator to poleward and drives the climate of tropics
9 and extratropics. Hence, the main purpose of studying the magnitude of ENSO events is to
10 investigate the impact of El Niño/La Niña strength on the Hadley circulation and subsequent
11 temperature and precipitation distribution at the global and regional scale focusing on the tropics
12 and extratropics. We will also revisit ENSO-induced variation in temperature and precipitation over
13 the Middle East and North Africa (MENA) with focus on Arabian Peninsula in winter season as this
14 region is getting attention and have been focused in many studies (Kucharski et al., 2013; Zeng and
15 Ning 2003, Giannini et al., 2008; Dogar, 2019) because of its sensitivity and drought-like response
16 to such events. In addition, we will focus on the model performance in replicating known facts of
17 ENSO teleconnection pattern over Pacific and Atlantic region such as ENSO-induced PNA pattern
18 over the Pacific as well as ENSO-induced NAO-like pattern in North Atlantic region and associated
19 climatic effects particularly in Europe and Middle East region.

20 Therefore, the current paper deals with the comparative study of ENSO teleconnection over ITCZ
21 and extratropical regions and its effect on rainfall, particularly in Africa and the Middle East
22 extending to the East Asian region. The study also deals with the ENSO-induced modulation (i.e.,
23 strengthening or weakening) of Hedley and Walker circulations that could initiate a significant
24 impact on Indian, Middle Eastern and African rainfall distribution. The rest of the paper is
25 organized as follows. Section 2 discusses material and methods including the description of the
26 model used in this study. Strong and weak ENSO episodes and their global and regional impacts in
27 the winter season are described in section 3. In the last Section, we summarized our results.

29 **2. Material and Methods**

30 **2.1 Model Description**

31 To study global and regional climate responses caused by ENSO forcing, we employed a
32 Geophysical Fluid Dynamics Laboratory global High-Resolution Atmospheric Model (GFDL-
33 HiRAM) effectively at 25 km horizontal grid resolution. The HiRAM model uses a cubed-sphere
34 finite-volume dynamical core that is based on GFDL's Atmospheric Model version 2 (AM2;
35 *Putman and Lin, 2007; Anderson et al., 2004*) with increased horizontal and vertical resolutions (32
36 vertical layers instead of 24 for better representation of stratospheric processes and its coupling with
37 the troposphere), as well as simplified parameterizations for moist convection and large-scale

1 stratiform cloudiness. HiRAM uses a new grid-point dynamical core along with a prognostic cloud
2 scheme, multi-species aerosol climatology as well as components from previous models used at
3 GFDL. However model retains the surface flux, land surface, gravity wave drag, boundary layer,
4 radiative transfer modules, and large-scale cloud microphysics of AM2 (*Anderson et al. 2004; Zhao*
5 *et al. 2009*). Soil processes considered in HiRAM are calculated using a land model known as LM3
6 that includes soil sensible and latent heat storage, groundwater storage, and stomata resistance
7 (*Anderson et al., 2004*).

8 The shortwave (SW) radiation processes are calculated using Freidenreich and Ramaswamy (1999)
9 algorithm. The SW radiation spectrum ranges from 0.17 to 4.0 μm , which is divided into 25 bands,
10 10 in the near IR region, 4 bands in the visible and 11 bands in the UV region and includes
11 absorption by H_2O , CO_2 , O_3 , O_2 as well as Rayleigh scattering. The longwave (LW) radiation code
12 is based on a modified form of the simplified exchange approximation (*Schwarzkopf and*
13 *Ramaswamy, 1999*). It accounts for the absorption and emission by the principal gases present in
14 the atmosphere including H_2O , O_3 , CO_2 , N_2O , CH_4 , and the halocarbons CFC-11, CFC-12, CFC-
15 113, and HCFC-22. Aerosols and clouds are treated as absorbers in the longwave, with non-grey
16 absorption coefficients specified in the eight spectral bands of the transfer scheme, following the
17 methodology adopted in Ramachandran et al. (2000). A detailed description of the HiRAM model
18 and related publications is available at <http://www.gfdl.noaa.gov/HiRAM>.

19 20 **2.2 Experimental Design and Methodology**

21 In this study, we used HiRAM simulations at C360 (~25 km) horizontal resolution, typically a range
22 that most of the regional climate models (RCMs) use in climate downscaling. This allows us to
23 study global and regional climatic processes using a global climate model (GCM) that fully
24 accounts for regional and global scale interactions, which are especially important in the tropics.
25 The model is forced with observed monthly SST from the Hadley Centre Sea Ice and Sea Surface
26 Temperature (HadISST) data set (*Rayner et al., 2003*). Three parallel simulations each of 33 years
27 simulation period (1976-2008) are conducted by taking into account greenhouse gases and volcanic
28 forcing. The aerosol spatial time distribution and optical characteristics of volcanic aerosols (that
29 were released by the volcanic eruption events in the simulation period) are calculated following
30 Stenchikov et al. (2006). To reduce the uncertainty (due to internal noise) in the model results, an
31 ensemble averaging over three HiRAM realizations is used. These three realizations were produced
32 using different initial conditions obtained from several integrations of the atmosphere-only model.
33 The first realization uses SST of Jan 1976, whereas second and third realizations use Jan 1977 and
34 Jan 1978 respectively from HadISST. In order to avoid spin-up effects, first three years of the
35 integration (1976-1978) in each realization are not included in the analysis. Model is run in
36 Atmospheric Model Inter-comparison Project (AMIP) mode with observed SST and sea ice
37 concentration determined from the HadISST data set. The sea-ice model assumes that each grid-

1 point is either fully ice-covered or ice-free and also considers a uniform ice thickness of 2 meters.

2 Anthropogenic greenhouse gases (GHGs), natural forcings, ozone, landuse and other possible
3 forcings data set (anthropogenic aerosols concentration in the atmosphere etc.) used in the model
4 follows AMIP historical simulation setup.

5 For comparison of the HiRAM response, we used NCEP-climate forecast system reanalysis (CFSR)
6 data. CFSR is a high-resolution reanalysis data produced using NCEP coupled atmosphere-ocean-
7 land surface-sea ice model (coupled with GFDL MOM version 4 and a two-layer sea ice model).
8 Most of the available in-situ and satellite observations are included in the CFSR. Satellite
9 observations are used in form of radiance, rather than retrieved values, and are bias-corrected with
10 “spin up” runs at full resolution. It is a recent NCEP reanalysis data that assimilates surface
11 observations, satellite radiances, CO₂, aerosols (including volcanic aerosols), and solar variations
12 using a high-resolution atmospheric model at T382 (~38 km) horizontal resolution with 64 vertical
13 levels ranging from the surface to 0.26 hPa. Annual averages of time-varying CO₂ concentration
14 including other radiatively absorbing gases; stratospheric volcanic aerosols and downward solar
15 radiation flux in CFSR are specified as described in Saha et al. (2010).

16 The ocean effect is included as we used observed SST that takes into account the ocean feedback. It
17 is not interactive, but it allows us to correctly account for such an aspect of natural variability as El
18 Niño. Typically, coupled models could have a problem in correctly reproducing the phase and
19 magnitude of the ENSO, so in this case we have an “ideal” observed SST forcing. Using
20 atmospheric model with the prescribed SST is, of course, an idealized approach, but fairly
21 reasonable one, as demonstrated in previous studies (Stenchikov et al., 2002; Dogar et al., 2017b).
22 The ocean effect in our simulations is not interactive but it is not absent. The observed SSTs, used
23 in the calculations, account for the ocean effect. Thus, in our simulations the atmospheric response
24 is fully interactive, and is constrained by observed ocean boundary conditions. This approach
25 allows us to more reliably evaluate the contributions of different processes and compare our results
26 with observations.

27 For strong El Niño episodes, we composited all the winter (DJF) seasons during the period 1979-
28 2008 that have SST anomaly equal or greater than 1.5 K over the Nino3.4 region. Whereas for the
29 case of weak El Niño, we composited all the winter seasons with SST anomaly with magnitude 0.5
30 to 1.5 K. For the case of La Niña, a same approach is applied, however, the SST anomaly values
31 over the Nino3.4 region is negative. For details regarding strong or weak ENSO episodes, the
32 readers may visit the link <https://ggweather.com/enso/oni.htm>. As ENSO predominantly
33 triggers/peaks in winter, therefore, we have presented anomalous signals for strong and weak ENSO
34 episodes in boreal winter (DJF) season only. The impact of stronger and weaker ENSO magnitude
35 is calculated as a simple departure of the stronger and weaker El Niño and La Niña composited
36 averages from the long-term winter (DJF) climatology that includes all the El Niño and La Niña
37 events in the simulation period (1979-2008) and roughly corresponds to neutral phase. The HiRAM

1 simulation results are compared with a high-resolution CFS Reanalysis (CFSR) product.

2

3 **3. Results and Discussion**

4 Before examining the impacts of strong and weak ENSO forcing at the global and regional scale,
5 we assessed the performance of HiRAM AGCM. Figure 1 shows the climatology pattern of 2m
6 surface temperature and rainfall superimposed with wind vectors produced using CFSR and
7 HiRAM model. These climatology maps clearly show that HiRAM model reproduces both
8 qualitatively and quantitatively the basic features of temperature and precipitation very well. The
9 convergence zones and cyclonic flow patterns in the Northern Hemisphere shown by zonal and
10 meridional wind vectors are well captured by the model simulation. This comparison increased our
11 confidence in the HiRAM simulation that motivated us to use this model for the assessment of
12 ENSO magnitude at the global and regional scale. Therefore, to have a better representation of the
13 ENSO-induced teleconnection patterns, we analyzed anomalous atmospheric responses following
14 the El Niño and La Niña events composited over the period of 1979-2008 (see methodology), as
15 discussed in the following sections.

16

17 **3.1 Strong ENSO Winter Impacts**

18 Figure 2 shows the global anomalous response of surface temperature at 2m following strong El
19 Niño and La Niña forcing in CFSR and HiRAM. Both the HiRAM and CFSR results show strong
20 warming over the eastern part of the tropical Pacific extending towards North America (Eastern and
21 Central America) as well as over Eurasia with strong cooling anomalies in the western Pacific
22 Ocean as well as over the Arctic Ocean. This El Niño-induced warming pattern seen in the tropical
23 Eastern Pacific extending further into North Pacific and Central American region resembles a well-
24 known horseshoe-like warming pattern. We also observed strong warming over parts of
25 Southwestern Europe, Southern Africa, the Indian Ocean, and Australia. We noticed that the model
26 well reproduced the observed features at the global scale with slight underestimation of the cooling
27 signal over the Arctic region as well as the Arabian Peninsula and North Africa. This
28 underestimation could be accounted for due to HiRAM weak response to ENSO-induced
29 stratospheric polar vortex variation (i.e., weakening or strengthening) following El Niño/La Niña
30 events and associated NAO-like pattern. The stratospheric polar vortex and associated NAO-like
31 response are underestimated in HiRAM, like other global models, and therefore the associated
32 temperature (i.e., cooling) response following El Niño in the high-latitude (i.e., mid-latitude and
33 polar regions) is underestimated in HiRAM compared to CFSR. Polar vortex is a stratospheric
34 phenomenon that is transported to surface through tropospheric–stratospheric interactions. These
35 polar vortex changes (strengthening or weakening) following ENSO events effects polar jets that in
36 turn produce strong changes in the mid-latitude and polar regions. HiRAM has a lower model top
37 (that covers lower stratosphere, model top reaches 10 hPa) compared to CFSR (that covers entire

1 stratosphere, model top reaches 0.1 hPa), which could be one of the reason that the HiRAM
2 underestimates weakening (i.e., breakdown) or strengthening of polar vortex and associated
3 circulation changes following internal or external climate forcing (Dogar, 2018; DallaSanta et al.,
4 2019; Marathe & Karumuri, 2021; Dogar, 2019). Further discussion regarding HiRAM
5 underestimation to ENSO forcing can be seen in supplementary Fig. S1 and S2. A reverse
6 anomalous pattern is roughly observed following strong La Niña episode both in the HiRAM and
7 NCEP-CFSR except over the Arabian Peninsula as well as over North America and Eurasia where
8 the cooling or warming signals are not anti-symmetric following strong El Niño and La Niña
9 episodes. This ENSO-induced (El Niño/La Niña) tropical warming/cooling pattern outspreading to
10 the Arctic and North American region is caused by a well-known ENSO-induced tropically excited
11 Arctic warming/cooling mechanism following the strong El Niño/La Niña events. In this tropically
12 excited Arctic mechanism, the pole-ward propagating Rossby waves can warm/cool the Arctic
13 region through adiabatic warming/cooling mechanism, an enhanced pole-ward stationary eddy heat
14 transport, and downward infrared radiation (Saravanan, 1993; Lee et al. 2012).

15 We also noticed a strong El Niño/La Niña-induced cooling/warming pattern over
16 Northern/Southern Africa that could be accounted for by large-scale dynamic circulation and
17 associated diabatic processes driven by Walker circulation and its transport from the tropics towards
18 extratropics through the latitudinal thermal gradient. Another mechanism of this African continental
19 cooling/heating could be explicated through convectively generated Rossby waves. These waves
20 emanate from the equatorial Pacific, moving eastward in circular paths resulting in wind and
21 pressure changes that play a key role in the transport of heating or cooling anomalies in the tropics
22 and outside the tropics (Jin and Hoskin 1995; Servan, 1993; Kiladis et al. 2009; Lee, 2012).
23 Temperature anomalies induced by strong El Niño forcing are very much consistent between the
24 model and CFSR. The anomalous 2m-temperature response following the La Niña forcing is
25 roughly opposite to the El Niño forcing. It suggests that the La Niña forcing will induce stronger
26 cooling over North America, Europe, Arabian Peninsula, and the African domain. From the spatial
27 anomaly pattern of surface temperature at 2m, we noticed that the HiRAM model reproduces the
28 impact of ENSO over the Pacific, North and South America very well and our results are consistent
29 with earlier studies (Sterl et al. 2007; Lee, 2012; Wang et al. 2012). However, it underestimates
30 ENSO teleconnection pattern and associated changes over the Middle East and North Africa
31 particularly over the Arabian Peninsula region, covering the Red Sea which could be accounted for
32 by the variations of ENSO-induced circulation changes (e.g., PNA and NAO) that could not be well
33 reproduced by the model as it has been noticed that the HiRAM model, like other up-to-date climate
34 models, underestimates the response of NAO in winter (Dogar, et al., 2017b; Driscoll et al., 2012).

35 Figure 3 shows the response of precipitation in winter season following strong El Niño and La Niña
36 events. The pattern of precipitation anomaly following both the El Niño and La Niña shows a
37 stronger signal over the tropics compared to extratropics. The spatial pattern of precipitation

1 anomaly (mm/d) reveals that El Niño forcing causes an increase in precipitation over the east and
2 central equatorial Pacific region and a decrease in precipitation in the western Pacific. This is
3 consistent with the warm anomaly in the east and central equatorial Pacific and cold anomalous
4 signal in the western Pacific Ocean, respectively, as observed in the 2m-temperature pattern (Figure
5 2). These warm (cold) surface features produce more (less) moisture transport that result in
6 increased (decreased) rainfall anomalies over the equatorial regions. We find that the strong El Niño
7 (La Niña) forcing typically reduce (intensifies) precipitation over the southern Africa in particular
8 southeastern region, resulting in dry (wet) conditions, while increasing (reducing) precipitation over
9 the northeastern tropical region.

10 We also noticed that El Niño-induced warm anomaly over the tropics causes more precipitation
11 over the ascending branch (i.e., ITCZ) of the Hadley cell. Subtropical regions that fall within the
12 downward or sinking branch of Hadley cell exhibit reduced precipitation anomalies which are very
13 much in agreement among CFSR and HiRAM. Since the latitudinal position of the rising and
14 sinking limbs of local Hadley cell varies at the regional scale, therefore increasing and decreasing
15 pattern of precipitation anomalies over the tropical region corresponds to the position of the ITCZ at
16 the regional scale.

17 A positive precipitation anomaly and cyclonic circulation response are seen near the California
18 coast and Aleutian region as well as in the Gulf of Mexico, Cuba, and Florida region, extending
19 further into the western Atlantic. El Niño also causes a decrease in precipitation over Bay of
20 Bengal, Sri Lanka, Thailand, Australia, and Columbia. This ENSO-induced winter precipitation
21 anomaly for the El Niño forcing is consistent with earlier studies showing a comparison of
22 precipitation anomaly between NCEP reanalysis and SPEEDY AGCM by regressing the
23 normalized Nino3.4 index with winter precipitation (Sterl et al. 2007; Kucharski et al. 2013). The
24 overall pattern of ENSO-induced precipitation changes over global and regional scale is well
25 reflected in HiRAM simulation and is in good agreement with CFSR and earlier studies (Dogar et
26 al., 2017a; Kucharski et al., 2013). Precipitation anomalies for La Niña conditions are roughly
27 opposite to that of El Niño. A dipole pattern of precipitation anomalies in high-latitudes (between
28 30-60°N and 30-60°S) following both El Niño and La Niña forcing could be associated with the
29 ascending and descending branch of the Ferrell cell.

30 In order to have a better idea of ENSO-induced changes in the tropical Hadley circulation, we have
31 plotted vertical velocity (Omega in Pa/sec) overlaid with ascending and descending air produced by
32 globally zonal averaged meridional and vertical wind profile [Fig. 4]. These results suggest that
33 both the El Niño and La Niña induce strong impact over the tropical atmospheric Hadley circulation
34 as both the vertical velocity and the intensity of the wind vectors have increased significantly
35 following strong El Niño event. We further noticed that strong El Niño forcing induces
36 strengthening and equatorward shift to Hadley cell (sinking limbs are stronger and confined within
37 10-25° latitude in both hemisphere) whereas the La Niña causes weakening to the Hadley cell

1 circulation. The structure of zonally averaged zonal wind anomaly following El Niño and La Niña
2 episode in winter season shows that the El Niño produces strengthening and equatorward shifting to
3 the jet streams (not shown). This ENSO-induced strengthening and equatorward shift of jet streams
4 leads to a narrower but intense Hadley cell circulation (Figure 4) because of increased eddy stress
5 (Lee, 2012). The response of Hadley cell to La Niña forcing is almost opposite to El Niño forcing.
6 Figure 5 presents ENSO-induced changes in tropical Walker circulation which shows consistent
7 pattern of rising and sinking limbs between CFSR and HiRAM. These El Niño-induced rising
8 patterns of the wind vectors over the tropical Pacific and the tropical Indian Ocean match with El
9 Niño-induced sea surface temperature (SST) warming in the tropical Pacific and the tropical Indian
10 Ocean (Figure 2). This ENSO-induced perturbation of the Walker circulation causes major shifts in
11 atmospheric circulations, rainfall patterns, and seasonal climate around the globe.

12 Figure 6 shows the response of geopotential height anomaly at 850 hPa following strong El Niño
13 and La Niña phases from HiRAM and NCEP-CFSR in winter (DJF) season. During strong El Niño
14 forcing geopotential height at 850 hPa shows a strong negative anomaly over the high-latitude
15 region (between 30-60N) in the Pacific Ocean extending towards the Atlantic ocean and a signature
16 of high anomalies over rest of the tropical belt particularly over the Indian Ocean focusing the
17 Arabian Sea that extends further to land areas of Africa, South, and Southeast Asia (Sterl et al.,
18 2007). Similarly, we observed signature of negative anomalies in high-latitude northern polar
19 regions and positive anomalies in the Southern Ocean. The anomaly of significant high and low
20 pressure further elongates zonally to the Atlantic Ocean and resembles a positive NAO-like
21 anomalous pattern over the Atlantic Ocean (Zhang et al. 2015). This positive NAO-like pattern will
22 produce a significant impact over Northern and Southern Europe extending to the Middle East and
23 North African region and induces cold and wet anomalies as seen in 2m surface temperature and
24 precipitation (Fig. 2 and Fig. 3 respectively) patterns (Shindel et al. 2004; Yu and Zhou, 2004;
25 Fischer et al. 2007). The mechanism that could explain this positive NAO-like pattern and
26 associated effects over Europe focusing southern Europe, Arabian Peninsula and North African
27 domain is caused by the convectively generated coupled Rossby waves (Saravanan, 1993; Jin and
28 Hoskins, 1995; Kiladis et al. 2009; Lee, 2012). The La Niña phase also displays a positive NAO-
29 like pattern over the North Atlantic region that will also result in cooling and drying anomalies over
30 Southern Europe and MENA region. Interestingly, the ENSO-induced NAO-like response over the
31 North Atlantic Ocean is more pronounced in the CFSR results than in HiRAM therefore associated
32 changes over Europe and MENA are also slightly underestimated in HiRAM response. These
33 results reveal that the climatic impacts of ENSO over the global and regional scale are very
34 sensitive to the intensity of ENSO and its warming and cooling phase in the tropical Pacific Ocean.
35 The geopotential height response and associated climatic patterns in the North Pacific are caused as
36 a result of a well-known boreal winter ENSO teleconnection pattern induced by the Rossby wave

1 source in the tropics that propagates towards extra-tropics and forms a quasi barotropic structure.
2 This wave train effect projects onto the Pacific North American (PNA) pattern, and the Aleutian
3 low. This prominent teleconnection associated with ENSO (El Niño/La Niña) events has been
4 referred to as the PNA pattern accompanied by an intensified Aleutian low during ENSO warm (El
5 Niño) phase. Corresponding to the ENSO (La Niña) cold phase, a positive geopotential height
6 anomaly covers the North Pacific indicating a weakened Aleutian Low during the La Niña events.
7 This type of pattern is anticipated to induce energy transport among tropics, extra-tropics and high-
8 latitude regions following El Niño and La Niña forcing (Lee, 2012). Figure 7 shows the pattern of
9 geopotential height anomaly at 200 hPa following strong El Niño and La Niña forcing. This upper
10 level geopotential height anomaly is high in the tropics and low in the subtropical region because
11 the positive ENSO phase (El Niño) overall warms the tropical atmosphere. This leads to high
12 geopotential height anomalies at the upper levels as a result of hydrostatic equilibrium. The
13 geopotential height is lower in the more northern latitudes because of wave propagations of various
14 types. This upper-level geopotential height anomaly is stronger over the tropical Pacific Ocean
15 compared to the rest of the tropical regions, which is associated with the El Niño-induced strong
16 tropical Pacific warming pattern. These results are qualitatively consistent with observational,
17 reanalysis and model based studies showing Nino3.4 regressed anomalous pattern of geopotential
18 height changes (Sterl et al. 2007; Kucharski et al. 2013; Dogar et al., 2017a). Responses of
19 geopotential height anomalies following strong La Niña episodes display a mirror image to their El
20 Niño counterparts.

21 **3.2 Weak ENSO Winter Impacts**

22 Figure 8 shows the global anomalous response of 2m surface temperature following weak El Niño
23 and La Niña forcing in CFSR and HiRAM. Both the HiRAM and CFSR results show strong
24 warming over the tropical eastern Pacific extending towards North America (Eastern and Central
25 America) as well as over Eurasia with weak cooling signatures in the Western Pacific and Arctic
26 Oceans. We also noticed a strong warming pattern over parts of South Western Europe, Africa, the
27 Indian Ocean, and Australia. Model is reproducing the observed features very well at the global
28 scale with underestimation of the cooling signal over Eurasia. A circumpolar westerly jet, confining
29 the coldest temperatures over the Arctic, characterizes the wintertime stratospheric polar vortex.
30 This underestimation could be accounted for by the strength of ENSO-induced stratospheric polar
31 vortex and associated circulation changes (supplementary Figs. S1 and S2). The stratospheric polar
32 vortex in winter and associated tropospheric and surface circulations (e.g., polar jets and NAO-like
33 response at surface) are underestimated in HiRAM, and therefore the warming/cooling response
34 following weak El Nino/La Nina in the Eurasian region is not well captured by HiRAM compared
35 to CFSR. We also observed differences over northern Europe and the northern part of Eurasia
36 where the HiRAM model shows strong cooling compared to CFSR, which shows warming. A

1 reverse anomalous pattern is roughly observed following weak La Niña episode both in the model
2 and NCEP-CFSR except the Eurasian region where we saw strong warming in Model results and
3 cooling response in CFSR. Moreover, the cooling signal over the North American region following
4 weak La Niña is stronger in the CFSR results whereas it is weaker in the HiRAM results. These
5 results suggest that the HiRAM model struggles in reproducing the teleconnection response for
6 weaker ENSO, especially over Eurasia, parts of the Arabian Peninsula, and America. This ENSO
7 (El Niño/La Niña)-induced tropical warming/cooling pattern extending to the Arctic and North
8 American region is caused by a well-known ENSO-induced tropically excited Arctic
9 warming/cooling mechanism following the El Niño/La Niña forcing. In this tropically excited
10 Arctic mechanism, the pole-ward propagating Rossby waves can warm/cool the Arctic through
11 adiabatic warming/cooling mechanism, an enhanced pole-ward stationary eddy heat transport, and
12 downward infrared radiation (Saravanan, 1993; Lee et al., 2012). We noticed that the La Niña
13 forcing induces a stronger cooling over the tropical central Pacific that propagates to North
14 America, Europe, Arabian Peninsula, and South Africa. From the spatial anomaly pattern of 2m
15 surface temperature, we noticed that the HiRAM model reproduces the impact of ENSO over the
16 Pacific, North and South America reasonably well and simulated results are in agreement with
17 earlier studies (Lee, 2012; Wang et al., 2012; Sterl et al., 2007), however, it underestimates and
18 gives feeble responses to weak ENSO teleconnection pattern and associated changes over the Indian
19 subcontinent, Eurasia, parts of Southern Europe, Northern and Central America, parts of Arabian
20 Peninsula including the Red Sea, which could be accounted for by the variations in stratospheric
21 and tropospheric aerosol impact caused by two major eruptions falling in the simulation period
22 during ENSO events. It could also be attributed to ENSO-induced circulation changes (e.g., NAO)
23 that like other models are not well reproduced by HiRAM (Driscoll et al., 2012; Dogar et al.,
24 2017b).

25 Figure 9 shows the response of precipitation anomaly (mm/d) in the winter season following weak
26 El Niño and La Niña events. The pattern of precipitation anomaly following both El Niño and La
27 Niña shows a stronger signal over the tropics compared to extratropics. The spatial pattern of
28 precipitation anomaly indicates that El Niño forcing is causing an increase in precipitation over the
29 east and central equatorial Pacific region and decreased precipitation in the western Pacific. This is
30 consistent with the warm anomalous pattern in the east and central equatorial Pacific and cold
31 anomalous pattern in the western equatorial Pacific respectively as observed in 2-m surface
32 temperature pattern (Figure 8). These warm (cold) surface features cause more (less) moisture
33 convergence, resulting in increased (decreased) rainfall anomalies over the equatorial regions. We
34 also noticed that El Niño induced warm anomaly over the tropics causes more precipitation over the
35 upward branch (i.e., ITCZ) of the Hadley cell. Subtropical regions that fall within the descending or
36 sinking branch of Hadley cell display reduced precipitation anomalies which are very much in

1 agreement among CFSR and HiRAM. As the latitudinal position of the ascending and descending
2 limbs of local Hadley cell varies at the regional scale (Schwendike, 2014), therefore, the increase
3 and decrease in precipitation anomalies over the tropical region follow the position of ITCZ at the
4 regional scale. The overall pattern of precipitation changes caused by ENSO on the global and
5 regional scale is well reflected in HiRAM simulation, and it is in good agreement with CFSR and
6 earlier studies (Kucharski et al. 2013). The precipitation anomalies obtained for La Niña conditions
7 are roughly opposite to El Niño impact, however, we noticed some differences in the model
8 responses especially following weak La Niña that could be accounted for by model underestimation
9 to circulation changes (Dogar and Sato, 2018; 2019).

10 To have a better idea of weak ENSO-induced changes in the tropical Hadley circulation, the vertical
11 velocity (Omega in Pa/sec) overlaid with rising and sinking air produced by globally zonal averaged
12 meridional and vertical wind profile are plotted (Fig. 10). These results reveal that, similar to strong
13 ENSO, both the weak El Niño and La Niña also induce a strong impact on the Hadley circulation as
14 both the vertical velocity and the intensity of the wind vectors have increased significantly
15 following the weak El Niño event. We further find that the El Niño induces strengthening and
16 equatorward shift of Hadley cell (i.e., sinking limbs are strong and confined within 10-25° latitude
17 in both hemispheres) whereas La Niña causes a reverse pattern. Although the model well captures
18 the rising and sinking branches of the Hadley cell, nevertheless the intensity is much weaker in the
19 model response compared to the CFSR. The pattern of zonally averaged zonal wind anomaly
20 following El Niño and La Niña episodes in the winter season shows that the El Niño forcing
21 produces strengthening and equatorward shift to the jet streams (not shown). This ENSO-induced
22 strengthening and shift of jet streams towards equator result in a narrower but intense Hadley cell
23 (Figure 4) because of increased eddy stress. The results of Hadley cell response to La Niña are
24 almost opposite to El Niño forcing. Figure 11 presents ENSO-induced changes in tropical Walker
25 circulation, which show a consistent pattern of rising and sinking limbs between CFSR and
26 HiRAM. However, the intensity of the model response is much weaker compared to CFSR and
27 there also exist some variations such that the model shows a rising pattern at 60°W while the
28 reanalysis shows a mixed pattern.

29 Figure 12 shows the response of geopotential height (GH) anomaly at 850 hPa following weak El
30 Niño and La Niña phases from HiRAM and NCEP-CFSR in the winter season. The geopotential
31 height at 850 hPa following weak El Niño forcing shows a negative anomaly structure over the
32 high-latitude region (between 30-60°N) in the Pacific and North Atlantic Oceans. A signature of
33 positive anomalies is seen over the tropical belt particularly over the Indian Ocean focusing the
34 Arabian Sea that extends further to land areas such as Australia, Africa, South Asia, and Southeast
35 Asia (Sterl et al. 2007). Similarly, we observed negative anomaly signature in the Arctic region and

1 slight positive anomaly signature in the Antarctic region (especially in the HiRAM response)
2 following the weak El Niño. The anomaly of high and low pressure over the Pacific region
3 elongates zonally to the Atlantic Ocean and resembles a positive NAO-like pattern over the Atlantic
4 Ocean (Zhang et al. 2015). However, the magnitude of this geopotential height anomaly is weak
5 following weak ENSO forcing. This positive NAO-like pattern produces significant impacts over
6 Northern and Southern Europe, extending to the MENA region, with cold and wet anomalies as
7 seen in 2m surface temperature and precipitation (Fig. 8 and Fig. 9 respectively). However, the
8 magnitude of these responses is much weaker. This NAO-like pattern and associated effects over
9 Europe focusing southern Europe, Arabian Peninsula, and North African domain is caused by
10 convectively generated coupled Rossby waves (Lee, 2012; Jin and Hoskins, 1995; Kiladis et al.
11 2009). The La Niña phase also exhibits a positive NAO-like pattern in the North Atlantic region,
12 leading to cooling and drying anomalies in Southern Europe and MENA region. Nevertheless,
13 HiRAM does not well capture this NAO-like response and gives different pattern following weak
14 La Niña event. As explained earlier, the ENSO-induced geopotential structure that resembles NAO-
15 like response over the North Atlantic Ocean is more pronounced in CFSR than HiRAM, so the
16 associated changes over Europe and MENA are also slightly underestimated in the HiRAM
17 response. Moreover, the responses both following El Niño and La Niña are somehow varying
18 between HiRAM and CFSR. These results suggest that the climatic impacts of ENSO on the global
19 and regional scales are very sensitive to the intensity of ENSO in the tropical Pacific. The
20 geopotential height response in the North Pacific is caused as a result of a well-known winter ENSO
21 teleconnection pattern induced by the Rossby wave source in the tropics that propagates towards
22 extra-tropics and forms a quasi barotropic structure. This wave train effect is weaker following
23 weak ENSO episodes. Therefore, the PNA and NAO-like structures observed after strong ENSO
24 episodes are not much obvious after weak ENSO episodes. Figure 13 shows the pattern of
25 geopotential height at 200 hPa following weak El Niño and La Niña forcing. The response of
26 geopotential anomaly at the tropical Pacific region resembles the Matsuno-Gill type pattern in the
27 tropical Central Pacific (Gill, 1980). However, its magnitude following weak ENSO forcing is
28 weaker than strong ENSO forcing. This upper-level geopotential height anomaly following El
29 Niño/La Niña is high/low in the tropics and low/high in the subtropics because the positive/negative
30 ENSO phase overall warms/cool the tropical atmosphere. This leads to high/low geopotential
31 anomalies in the upper levels as a result of hydrostatic equilibrium. The height is lower in the more
32 northern latitudes because of wave propagations of various types. This upper-level geopotential
33 height anomaly is stronger over the tropical Pacific compared to the rest of the tropics, which is
34 associated with the El Niño-induced tropical Pacific warming pattern. These results are qualitatively
35 consistent with earlier observational and modeling studies showing Niño3.4 regressed anomalous
36 pattern of geopotential height changes (Dogar et al., 2017a; Kucharski et al. 2013; Sterl et al. 2007).
37 We noticed that the response of the geopotential height anomaly following the La Niña episode

1 does not reflect a reverse pattern over the tropics or extratropics. Moreover, the response of model
2 is also not very similar to CFSR over high-latitude regions in both hemispheres, especially in the
3 Arctic and Antarctic areas.

4 **3.3 Response of MENA and Asia to Strong and Weak ENSO**

5 To better highlight model response regional climate response of the HiRAM model to strong and
6 weak ENSO forcing, we looked at the response of 2m surface temperature and precipitation over
7 the MENA regions. We focused on the MENA and Asia, as these regions are among the most
8 sensitive regions and several studies previously used HiRAM model to better understand the
9 climate of these regions (Bangalath and Stenchikov, 2015; Dogar et al., 2017b; Dogar and Sato,
10 2018; 2019). Figure 14 shows the case of strong ENSO forcing over the MENA and Asian region.
11 ENSO-induced warming over Northern Europe, Russia, and the tropical Indian Ocean region and
12 cooling over Africa, the Middle East, and the Asian region is consistent among the reanalysis and
13 HiRAM. However, we noticed this warming and cooling structure is more pronounced in the
14 reanalysis compared to the model that could be associated with the global climate model's weak
15 response to ENSO-induced circulation changes (Dogar et al., 2017b; Dogar and Sato, 2018; 2019;
16 Robock, 2012; Timmreck 2012). The warming and cooling anomaly following strong La Niña is
17 also somehow consistent between the model and the reanalysis except for Central Africa, and India
18 where there appeared a different anomalous structure that could be associated to model weak
19 response to ENSO-induced circulation changes such as ENSO-induced NAO-like response. Figure
20 15 shows the precipitation changes over the MENA region following strong El Niño and La Niña
21 forcing. The strong El Niño forcing causes enhanced precipitation over the Arabian Sea and
22 decreased precipitation over the Bay of Bengal. The structure of precipitation response is largely
23 consistent between the HiRAM and the CFS reanalysis. However, there exists slight variation over
24 the Indian Ocean following the La Niña forcing. Moreover, we noticed that the response of weak
25 ENSO forcing on the MENA region is much different and the HiRAM model gives a different
26 structure of 2-m surface air temperature over Europe and the Eurasian region (Figure 16),
27 suggesting that the weak ENSO forcing response is not well reproduced by HiARM model over the
28 MENA and Asia. The structure of precipitation response, especially over Europe, India including
29 the Arabian Sea is also different between the model and the reanalysis following weak La Niña
30 forcing in the winter season (Figure 17). Supplementary Figures S1 and S2 and associated
31 discussion regarding HiRAM response to circulation changes could account for discrepancies/biases
32 between HiRAM and CFSR. This supplementary analysis highlights the importance/need of air-sea
33 coupling (for better simulation of ENSO-induced thermal changes) and enhanced model top (to
34 better account for stratospheric processes, e.g., polar vortex changes and NAO-like teleconnection).
35 Therefore, systematic improvements in GCMs are needed to better simulate ENSO-induced
36 circulation changes and associated climatic impacts especially for MENA region, which being part

1 of the Hadley cell, is sensitive to internal and external climate drivers (e.g., aerosol forcing or
2 internal variability). Due to low model top, vertical variations of stratospheric dynamics and the
3 impact of the stratospheric polar vortex are underestimated in HiRAM. Hence, by considering air-
4 sea coupling and increased model top in high-resolution AMIP-type simulations could improve the
5 biases between the observations and simulation following strong and weak ENSO forcing.

6 7 **4. Summary and Conclusions**

8 The present study is an attempt to evaluate the role of ENSO intensity (i.e., strong and weak El
9 Niño/La Niña) in causing global and regional climate changes using a very high-resolution
10 atmospheric model (HiRAM), effectively at 25 km grid spacing. HiRAM simulated responses to
11 ENSO strength using 2m surface temperature, precipitation, geopotential height and vertical wind
12 composited anomaly pattern following El Nino/La Nina during the period 1979-2008 are compared
13 with a high-resolution CFS reanalysis, which is available at 38 km grid spacing.

14 Earlier studies suggest that the intensity and frequency of ENSO events have increased over the last
15 few decades resulting in a need to study the global and regional climatic impacts of ENSO strength.
16 Although, the main progress on the study of ENSO events and their climatic impacts was initially
17 made using climate models of intermediate complexity. However, these intermediate complexity
18 models have a coarse resolution, limiting them to have a detailed analysis of ENSO-induced
19 climatic responses, especially at the regional scale. Hence, to better understand ENSO-induced
20 climatic impacts at the global to regional scale, we used a high-resolution atmospheric model,
21 HiRAM, developed at GFDL, effectively at 25 km grid resolution. We have analyzed the impact of
22 El Niño/La Niña magnitude on 2m surface temperature, precipitation, sea level pressure, vertical
23 wind, and geopotential height at the global and regional scale focusing on the tropical and
24 extratropical regions.

25 The results obtained using HiRAM atmospheric model show that ENSO has a stronger impact over
26 the Inter-tropical Convergence Zone (ITCZ) region compared to extratropics and high-latitude
27 regions. These results are largely consistent with the findings of Zhao et al. (2016) who showed that
28 the ocean forcing from the ENSO is secondary and tend to be confined in the tropics. However, the
29 study of Zhao et al., 2016 did not categorize ENSO into strong and weak ENSO events. We further
30 noticed that the strong ENSO positive phase causes a significant weakening of rainfall over Africa,
31 South Asia whereas the La Niña phase of strong ENSO produces more rain over these regions. The
32 model results also reveal that ENSO has a stronger impact over South Asia particularly over the
33 Indian region because of its significant impact over the Indian Ocean focusing on the Arabian Sea,
34 the Bay of Bengal, and the Laccadive Sea through the Walker circulation.

35 Analysis of precipitation anomalies, zonal-mean vertical wind, and geopotential height changes at
36 850 and 200 hPa, reveal that the ENSO magnitude significantly impacts Hadley and Walker
37 circulation. Model-based configuration of Hadley cell following strong and weak El Niño (La Niña)

1 events emphasizes that the intensity of Hadley rising and sinking branches increased (decreased)
2 significantly exhibiting that Hadley circulation is very sensitive to the magnitude of ENSO forcing.
3 ENSO-induced changes in precipitation and vertical wind profile suggest that strong ENSO positive
4 phase (El Niño) can induce strengthening and equatorward shrinking to Hadley cell whereas the
5 negative phase of strong ENSO (La Niña) causes weakening of tropical Hadley cell. These AMIP-
6 style HIRAM-based ENSO experiments further reveal that the strong El Niño (La Niña) induces
7 significant weakening (strengthening) to local Hadley cell covering MENA and Asian tropical
8 regions, which may cause weakening (strengthening) of Indian and African rainfall, indicating that
9 MENA and South Asian tropical regions are very sensitive to tropically excited SST changes. This
10 ENSO-induced strengthening and weakening of Hadley cell along with variations in Walker
11 circulation induce significant impact over tropical regions covering South and Southeast Asian and
12 African rain-belt regions. Our study reveals that strong El Niño (La Niña) episodes cause
13 strengthening (weakening) and equatorward (poleward) shift to jet streams.

14 Analysis of geopotential height (GH) changes suggests that ENSO-induced negative (positive)
15 NAO-like response and associated changes in Southern Europe and MENA region become
16 significantly strong following the increased intensity of El Niño (La Niña) in the northern
17 hemisphere in the boreal winter season. The HiRAM model reproduces the impact of ENSO over
18 the Pacific, North and South America, and African region quite well however it fails to accurately
19 produce ENSO teleconnection patterns and associated changes in temperature and precipitation
20 following weak ENSO events. One of the possible reasons for this disparity could be that the
21 ENSO-induced NAO-like response might be a key component that is not well reproduced by the
22 model.

23 Our study suggests that ENSO-induced changes in sea surface temperature over the tropical Indian
24 Ocean could play a significant role in governing teleconnections through changes in Walker
25 circulation that consequently induces changes in the meridional thermal gradient. This study further
26 concludes that SST forcing in the tropical Indian and the Pacific Ocean and their teleconnection
27 through large-scale zonal atmospheric overturning circulation is attributed to be a potentially
28 important driving condition for fully characterizing ENSO-induced climatic changes in South Asia.
29 In general ENSO-induced global and regional teleconnection patterns of surface temperature,
30 precipitation, sea level pressure (SLP) and geopotential height changes are consistent with CFSR as
31 well as with earlier studies, which indicates that the HiRAM model can be used effectively to better
32 understand ENSO-induced global and regional climatic responses.

33 The HiRAM model underestimated the cooling response following strong ENSO over the MENA
34 region that could be accounted for by HiRAM weak response to ENSO-induced NAO-like
35 teleconnection and associated regional impacts over MENA. We further find that the HIRAM
36 model well reproduced the Matsuno-Gill pattern and horseshoe-like pattern following strong ENSO,
37 however, these patterns are poorly reproduced following the weak ENSO phase resulting in varying

1 regional climatic impacts over the MENA, Eurasian, South, and Southeast Asian regions,
 2 suggesting that HiRAM based ENSO results are sensitive to ENSO strength. The use of the air-sea
 3 coupling and increased model top (to better reflect ENSO-induced polar vortex changes) in high-
 4 resolution AGCM simulations could improve these biases between observations and simulations
 5 following strong and weak ENSO events.

7 Acknowledgements

8 We would like to thank the editor and two anonymous reviewers whose constructive suggestions
 9 and comments significantly improved the manuscript. An updated description of the latest version
 10 of the model used in this study as well as previous model versions is available at
 11 <https://www.gfdl.noaa.gov/atmospheric-model/>.

12 References

- 14 1. Afzaal M, Li JP, Jin FF (2013). The asymmetric influence of the two types of El Niño
 15 and La Niña on summer rainfall over Southeast China. *J Clim* 26:4567–4582.
- 17 2. Ashok, K., Guan, Z., & Yamagata, T. (2001). Impact of the Indian Ocean dipole on the
 18 relationship between the Indian monsoon rainfall and ENSO. *Geophysical Research*
 19 *Letters*, 28(23), 4499-4502.
- 21 3. Ashok, K., Guan, Z., Saji, N. H., & Yamagata, T. (2004). Individual and combined
 22 influences of ENSO and the Indian Ocean dipole on the Indian summer monsoon.
 23 *Journal of Climate*, 17(16), 3141-3155.
- 25 4. Ashok K, Behera S, Rao AS, Weng HY, Yamagata T (2007) El Niño Modoki and its
 26 possible teleconnection. *J Geophys Res* 112:C11007. doi:10.1029/2006JC003798.
- 28 5. Barimalala, R., A. Bracco, and F. Kucharski, 2011: The representation of the South
 29 Tropical Atlantic tele- connection to the Indian Ocean in the AR4 coupled models.
 30 *Climate Dyn.*, doi:10.1007/s00382-011-1082-5.
- 32 6. Bhalme, H. N., & Mooley, D. A. (1980). Large-scale droughts/floods and monsoon
 33 circulation. *Monthly Weather Review*, 108(8), 1197-1211.
- 35 7. Bracco, A., Kucharski, F., Molteni, F., Hazeleger, W., & Severijns, C. (2007). A recipe
 36 for simulating the interannual variability of the Asian summer monsoon and its relation
 37 with ENSO. *Climate dynamics*, 28(5), 441-460.
- 39 8. Bulić, I. H., and Č. Branković (2007), ENSO forcing of the Northern Hemisphere
 40 climate in a large ensemble of model simulations based on a very long SST record,
 41 *Climate dynamics*, 28(2-3), 231-254.
- 43 9. Bulić, I. H., Branković, Č., & Kucharski, F. (2012). Winter ENSO teleconnections in a
 44 warmer climate. *Climate dynamics*, 38(7-8), 1593-1613.
- 46 10. Chung, C. T., Power, S. B., Arblaster, J. M., Rashid, H. A., & Roff, G. L. (2014). Nonlinear
 47 precipitation response to El Niño and global warming in the Indo-Pacific. *Climate Dynamics*,
 48 42(7-8), 1837-1856.

- 1 11. DallaSanta, K., Gerber, E. P., & Toohey, M. (2019). The circulation response to
2 volcanic eruptions: The key roles of stratospheric warming and eddy interactions.
3 *Journal of Climate*, 32(4), 1101-1120.
- 4 12. Diaz, H. F., M. P. Hoerling, and J. K. Eischeid (2001), ENSO variability,
5 teleconnections and climate change, *International Journal of Climatology*, 21(15),
6 1845-1862.
- 7
- 8 13. Dogar, M. M., Kucharski, F., & Azharuddin, S. (2017a). Study of the global and
9 regional climatic impacts of ENSO magnitude using SPEEDY AGCM. *Journal of Earth
10 System Science*, 126(2), 30.
- 11
- 12 14. Dogar, M. M., Stenchikov, G., Osipov, S., Wyman, B., & Zhao, M. (2017b). Sensitivity
13 of the regional climate in the Middle East and North Africa to volcanic perturbations.
14 *Journal of Geophysical Research: Atmospheres*, 122(15), 7922-7948.
- 15
- 16 15. Dogar, M. M., & Sato, T. (2018). Analysis of climate trends and leading modes of
17 climate variability for MENA region. *Journal of Geophysical Research: Atmospheres*,
18 123(23), 13-074.
- 19
- 20 16. Dogar, M. M. (2018). Impact of tropical volcanic eruptions on Hadley circulation using
21 a high-resolution AGCM.
- 22
- 23 17. Dogar, M. M. A. (2020). *Study of the regional climatic impacts of tropical explosive
24 volcanism in the Middle East and North Africa region* (Doctoral dissertation,
25 北海道大学).
- 26
- 27 18. Dogar, M. M. (2019). The Sensitivity of DTR to the increased CO₂ over Mid-latitude
28 Semi-dry Regions.
- 29
- 30 19. Dogar, M. M., Kucharski, F., Sato, T., Mehmood, S., Ali, S., Gong, Z., ... & Arraut, J.
31 (2019). Towards understanding the global and regional climatic impacts of Modoki
32 magnitude. *Global and Planetary Change*, 172, 223-241.
- 33
- 34 20. Dogar, M. M., & Sato, T. (2019). Regional climate response of Middle Eastern,
35 African, and South Asian monsoon regions to explosive volcanism and ENSO forcing.
36 *Journal of Geophysical Research: Atmospheres*, 124(14), 7580-7598.
- 37
- 38 21. Dogar, M. M. A., & Shahid, A. (2018, December). Sensitivity of Hadley circulation to
39 volcanic radiative forcing. In *AGU Fall Meeting Abstracts* (Vol. 2018, pp. A53M-
40 2672).
- 41
- 42 22. Dogar, M. M. A., & Shahid, A. (2019, December). Revisiting the Climatic Impacts of
43 ENSO Modoki Varying Magnitude. In *AGU Fall Meeting Abstracts* (Vol. 2019, pp.
44 GC31D-1221).
- 45
- 46 23. Feng, J., and J. Li (2013), Contrasting impacts of two types of ENSO on the boreal
47 spring Hadley circulation, *Journal of Climate*, 26(13), 4773-4789.
- 48
- 49 24. Fischer, E. M., J. Luterbacher, E. Zorita, S. F. B. Tett, C. Casty, and Wanner H. (2007),
50 European climate response to tropical volcanic eruptions over the last half millennium,
51 *Geophysical Research Letters*, 34(L05707), doi:10.1029/2006GL027992.
- 52

- 1 25. Frauen, C., Dommenges, D., Tyrrell, N., Rezný, M., & Wales, S. (2014). Analysis of
2 the nonlinearity of El Niño–Southern Oscillation teleconnections. *Journal of Climate*,
3 27(16), 6225-6244.
4
- 5 26. Giannini, A., Biasutti, M., & Verstraete, M. M. (2008). A climate model-based review
6 of drought in the Sahel: Desertification, the re-greening and climate change. *Global and*
7 *planetary Change*, 64(3), 119-128.
8
- 9 27. Gill, A. E., (1980). Some simple solutions for heat-induced tropical circulation. *Quart.*
10 *J. Roy. Meteor. Soc.*, **106**, 447-462.
11
- 12 28. Held, I. M., & Hou, A. Y. (1980). Nonlinear axially symmetric circulations in a nearly
13 inviscid atmosphere. *Journal of the Atmospheric Sciences*, 37(3), 515-533.
14
- 15 29. Hoerling, M. P., Kumar, A., & Zhong, M. (1997). El Niño, La Niña, and the nonlinearity of their
16 teleconnections. *Journal of Climate*, 10(8), 1769-1786.
17
- 18 30. Jin, F., & Hoskins, B. J. (1995). The direct response to tropical heating in a baroclinic
19 atmosphere. *Journal of the atmospheric sciences*, 52(3), 307-319.
20
- 21 31. Ju, J., & Slingo, J. (1995). The Asian summer monsoon and ENSO. *Quarterly Journal*
22 *of the Royal Meteorological Society*, 121(525), 1133-1168.
23
- 24 32. Kao, H. Y., & Yu, J. Y. (2009). Contrasting eastern-Pacific and central-Pacific types of
25 ENSO. *Journal of Climate*, 22(3), 615-632.
26
- 27 33. Kiladis, G. N., Wheeler, M. C., Haertel, P. T., Straub, K. H., & Roundy, P. E. (2009).
28 Convectively coupled equatorial waves. *Reviews of Geophysics*, 47(2).
29
- 30 34. Kug JS, Jin FF, An SI (2009) Two types of El Niño events: cold tongue El Niño and
31 warm pool El Niño. *J Clim* 22:1499–1515.
32
- 33 35. Kripalani, R., Oh, J., Kulkarni, A. et al. *Theor. Appl. Climatol.* (2007) 90: 133.
34 doi:10.1007/s00704-006-0282-0.
35
- 36 36. Kucharski, F., Molteni, F., & Bracco, A. (2006). Decadal interactions between the
37 western tropical Pacific and the North Atlantic Oscillation. *Climate dynamics*, 26(1),
38 79-91.
39
- 40 37. Kucharski, F., Molteni, F., & Yoo, J. H. (2006). SST forcing of decadal Indian
41 monsoon rainfall variability. *Geophysical research letters*, 33(3).
42
- 43 38. Kucharski, F., Bracco, A., Yoo, J. H., & Molteni, F. (2007). Low-frequency variability
44 of the Indian monsoon-ENSO relationship and the tropical Atlantic: The “weakening”
45 of the 1980s and 1990s. *Journal of Climate*, 20(16), 4255-4266.
46
- 47 39. Kucharski, F., Zeng, N., & Kalnay, E. (2013). A further assessment of vegetation
48 feedback on decadal Sahel rainfall variability. *Climate dynamics*, 40(5-6), 1453-1466.
49
- 50 40. Kucharski, F., Molteni, F., King, M. P., Farneti, R., Kang, I. S., & Feudale, L. (2013).
51 On the need of intermediate complexity general circulation models: a “SPEEDY”
52 example. *Bulletin of the American Meteorological Society*, 94(1), 25-30.
53
- 54 41. Kumar, K.K., Rajagopalan, B., and Cane, M, A., 1999a: On the weakening relationship
55 between the Indian monsoon and ENSO. *Science*, 284, 2156-2159.

- 1
2 42. Kumar, K.K., Kleeman R., Cane M. A., Rajagopalan B., 1999. Epochal changes in
3 Indian monsoon-ENSO precursors. *Geophys. Res. Lett.* 26, 75.
4
5 43. Larkin NK, Harrison DE (2005). On the definition of El Niño and associated seasonal
6 average U.S. weather anomalies. *Geophys Res Lett* 32:L13705.
7 doi:10.1029/2005GL022738.
8
9 44. Latif, M., R. Kleeman, and C. Eckert (1997), Greenhouse warming, decadal variability,
10 or El Niño? An attempt to understand the anomalous 1990s, *J. Clim.*, 10, 2221–2239,
11 doi:10.1175/1520-0442(1997)010<2221:GWDVOE>2.0.CO;2.
12
13 45. Lean, J. L., & Rind, D. H. (2008). How natural and anthropogenic influences alter
14 global and regional surface temperatures: 1889 to 2006. *Geophysical Research Letters*,
15 35(18).
16
17 46. Lee SK, Wang C, Enfield DB (2010) On the impact of central Pacific warming event
18 on Atlantic tropical storm activity. *Geophys Res Lett* 37:L17702.
19 doi:10.1029/2010GL044459
20
21 47. Lee, S. (2012). Testing of the tropically excited Arctic warming mechanism (TEAM)
22 with traditional El Niño and La Niña. *Journal of Climate*, 25(12), 4015-4022.
23
24 48. Lau, N. C., & Nath, M. J. (2000). Impact of ENSO on the variability of the Asian-
25 Australian monsoons as simulated in GCM experiments. *Journal of Climate*, 13(24),
26 4287-4309.
27
28 49. Lu, J., G. Chen, and D. M. W. Frierson, 2008: Response of the zonal mean atmospheric
29 circulation to El Niño versus global warming. *J. Climate*, 21, 5836–5851.
30
31 50. Marathe, S., & Karumuri, A. (2021). The El Niño Modoki. In *Tropical and Extratropical Air-*
32 *Sea Interactions* (pp. 93-114). Elsevier.
33
34 51.
35 52. Molteni F (2003) Atmospheric simulations using a GCM with simplified physical
36 parameterizations. I. Model climatology and variability in multi-decadal
37 experiments. *Clim Dyn* 20:175–191.
38
39 53. Molteni F, Corti S, Ferranti L, Slingo JM (2003) Predictability experiments for the
40 Asian summer monsoon: Impact of SST anomalies on interannual and intraseasonal
41 variability. *J Clim* 16:4001–4021.
42
43 54. Molteni, F., King, M. P., Kucharski, F., & Straus, D. M. (2011). Planetary-scale
44 variability in the northern winter and the impact of land–sea thermal contrast. *Climate*
45 *dynamics*, 37(1-2), 151-170.
46
47 55. Nguyen, H., A. Evans, C. Lucas, I. Smith, and B. Timbal (2013), The Hadley
48 circulation in reanalyses: Climatology, variability, and change, *Journal of Climate*,
49 26(10), 3357-3376.
50
51 56. Neelin, J. D., Battisti, D. S., Hirst, A. C., Jin, F. F., Wakata, Y., Yamagata, T., &
52 Zebiak, S. E. (1998). ENSO theory. *Journal of Geophysical Research: Oceans*, 103(C7),
53 14261-14290.

- 1 57. Pant, G.B. and Parthasarathy, B., 1981. Some aspects of an association between the
2 southern oscillation and Indian summer monsoon. *Arch. Meteorol. Geophys. Biokl., Sr.*
3 *B.*, 29, 245-251.
4
- 5 58. Parthasarathy, B., Rupa Kumar, K. and Munot, A.A., 1991b. Evidence of secular
6 variations in Indian summer monsoon rainfall-circulation relationships. *J. Climate*, 4,
7 927-938.
8
- 9 59. Parthasarathy, B., K. R. Kumar, D. R. Kothawale, Indian summer monsoon rainfall
10 indices: 1871–1990, *Meteorol. Mag.*, 121, 174–186, 1992.
11
- 12 60. Parthasarathy, B., A. A. Munot, D. R. Kothawale, All-India monthly and summer
13 rainfall indices: 1871–1993, *Theor. Appl. Climatol.*, 49, 219–224, 1994.
14
- 15 61. Rasmusson, E. M., & Carpenter, T. H. (1983). The relationship between eastern
16 equatorial Pacific sea surface temperatures and rainfall over India and Sri Lanka.
17 *Monthly Weather Review*, 111(3), 517-528.
18
- 19 62. Rosatki A., Miakoda K., Gudgel R., (1997) The Impact of Ocean Initial Conditions on
20 ENSO Forecasting with a Coupled Model. *Monthly Weather Review, Jour. of Amer.*
21 *Met. Soc.*, 125, 754-772.
22
- 23 63. Saravanan, R., 1993: Equatorial superrotation and maintenance of the general
24 circulation in two-level models. *J. Atmos. Sci.*, 50, 1211–1227.
25
- 26
- 27 64. Schwarzkopf, M. D., & Ramaswamy, V. (1999). Radiative effects of CH₄, N₂O,
28 halocarbons and the foreign-broadened H₂O continuum: A GCM experiment. *Journal*
29 *of Geophysical Research*, 104(D8), 9467–9488. <https://doi.org/10.1029/1999JD900003>.
30
- 31 65. Shindell, D. T., G. A. Schmidt, M. E. Mann, and G. Faluvegi (2004a), Dynamic winter
32 climate response to large tropical volcanic eruptions since 1600, *Journal of Geophysical*
33 *Research*, 109, doi:10.1029/2003JD004151.
34
- 35 66. Shukla, J., & Paolino, D. A. (1983). The Southern Oscillation and long-range
36 forecasting of the summer monsoon rainfall over India. *Monthly Weather Review*,
37 111(9), 1830-1837.
38
- 39 67. Singh, P., Chowdary, J. S., & Gnanaseelan, C. (2013). Impact of prolonged La Niña
40 events on the Indian Ocean with a special emphasis on southwest Tropical Indian
41 Ocean SST. *Global and planetary change*, 100, 28-37.
42
- 43 68. Seager, R., Harnik, N., Kushnir, Y., Robinson, W., & Miller, J. (2003). Mechanisms of
44 hemispherically symmetric climate variability*. *Journal of Climate*, 16(18), 2960-2978.
45
- 46 69. Sterl, A., van Oldenborgh, G. J., Hazeleger, W., & Burgers, G. (2007). On the
47 robustness of ENSO teleconnections. *Climate Dynamics*, 29(5), 469-485.
48
- 49 70. Schwendike, J., P. Govekar, M. J. Reeder, R. Wardle, G. J. Berry, and C. Jakob (2014),
50 Local partitioning of the overturning circulation in the tropics and the connection to the
51 Hadley and Walker circulations, *Journal of Geophysical Research: Atmospheres*,
52 119(3), 1322-1339.
53

- 1 71. Timmermann, A., Oberhuber, J., Bacher, A., Esch, M., Latif, M., & Roeckner, E.
2 (1999). Increased El Niño frequency in a climate model forced by future greenhouse
3 warming. *Nature*, 398(6729), 694-697.
4
- 5 72. Tokinaga, Hiroki, et al. "Slowdown of the Walker circulation driven by tropical Indo-
6 Pacific warming." *Nature* 491.7424 (2012): 439-443.
7
- 8 73. Trenberth, K. E., Branstator, G. W., Karoly, D., Kumar, A., Lau, N. C., & Ropelewski,
9 C. (1998). Progress during TOGA in understanding and modeling global
10 teleconnections associated with tropical sea surface temperatures. *Journal of*
11 *Geophysical Research: Oceans*, 103(C7), 14291-14324.
12
- 13 74. Trenberth KE, Caron JM (2000) The Southern Oscillation revisited: sea level pressure,
14 surface temperatures, and precipitation. *J Clim* 13:4358–4365
15
- 16 75. Walker, G. T. (1925). Correlation in seasonal variations of WEATHER-A further study
17 of world WEATHER 1. *Monthly Weather Review*, 53(6), 252-254.
18
- 19 76. Wang, C., Deser, C., Yu, J. Y., DiNezio, P., & Clement, A. (2012). El Niño and
20 southern oscillation (ENSO): a review. *Coral reefs of the Eastern Pacific*, 3-19.
21
- 22 77. Wu, R., Lin, M., & Sun, H. (2020). Impacts of different types of El Niño and La Niña
23 on northern tropical Atlantic sea surface temperature. *Climate Dynamics*, 54(9), 4147-
24 4167.
25
- 26 78. Wu, R., & He, Z. (2019). Northern tropical Atlantic warming in El Niño decaying
27 spring: Impacts of El Niño amplitude. *Geophysical Research Letters*, 46(23), 14072-
28 14081.
29
- 30 79. Wu, R., Chen, J., & Chen, W. (2012). Different types of ENSO influences on the Indian
31 summer monsoon variability. *Journal of Climate*, 25(3), 903-920.
32
- 33 80. Xie, S. P., Deser, C., Vecchi, G. A., Ma, J., Teng, H., & Wittenberg, A. T. (2010).
34 Global warming pattern formation: sea surface temperature and rainfall*. *Journal of*
35 *Climate*, 23(4), 966-986.
36
- 37 81. Yeh, S. W., Kug, J. S., Dewitte, B., Kwon, M. H., Kirtman, B. P., & Jin, F. F. (2009).
38 El Niño in a changing climate. *Nature*, 461(7263), 511-514.
39
- 40 82. Yu, J. Y., and S. T. Kim (2010), Three evolution, patterns of central Pacific El Niño,
41 *Geophys. Res. Lett.*, 37, L08706, doi:10.1029/2010GL042810.
42
- 43 83. Yu, R., & Zhou, T., 2004. Impacts of winter-NAO on March cooling trends over
44 subtropical Eurasia continent in the recent century. *Geophysical Research Letters*,
45 31(L12204). doi: 10.1029/2004GL019814.
46
- 47 84. Zhao, M., I. M. Held, S.-J. Lin, and G. A. Vecchi (2009), Simulations of global
48 hurricane climatology, interannual variability, and response to global warming using a
49 50-km resolution GCM, *Journal of Climate*, 22(24), 6653-6678.
50
- 51 85. Zhang, W. J., F.-F. Jin, J. P. Li, and H.-L. Ren, 2011: Contrasting impacts of two-type
52 El Niño over the western North Pacific during boreal autumn. *J. Meteor. Soc. Japan*, 89,
53 563–569.
54

- 1 86. Zhang WJ, Jin FF, Ren HL, Li JP, Zhao JX (2012). Differences in teleconnection over
 2 the North Pacific and rainfall shift over the USA associated with two types of El Niño
 3 during boreal autumn. *J Meteorol Soc Jpn* 90:535–552
 4
- 5 87. Zhang WJ, Jin FF, Zhao JX, Qi L, Ren HL (2013). The possible influence of a non-
 6 convective El Niño on the severe autumn drought of 2009 in Southwest China. *J Clim*
 7 26:8392–8405
 8
- 9 88. Zhang, W., Wang, L., Xiang, B., Qi, L., & He, J. (2015). Impacts of two types of La
 10 Niña on the NAO during boreal winter. *Climate Dynamics*, 44(5-6), 1351-1366.
 11
- 12 89. Zeng, N. (2003), Drought in the Sahel, *Science*, 302(5647), 999-1000.
 13

14 **Figure Legends:**

15 **Figure 1:** Composited mean spatial pattern of 2m surface air temperature (°C in top) and
 16 precipitation (mm/day in bottom) in winter season produced using CFSR (left panel) and HiRAM
 17 simulation (right panel). Wind vectors are also overlaid from CFSR (left bottom panel) and HiRAM
 18 (right bottom panel).

19 **Figure 2:** Composited mean 2m surface temperature anomaly pattern from HiRAM (left panel) and
 20 CFSR (right panel) following strong El Niño and La Niña forcing in winter (DJF) season.

21 **Figure 3:** Composited mean precipitation (mm/d) anomaly following strong El Niño and La Niña
 22 forcing in winter (DJF) season.

23 **Figure 4:** Composited mean anomaly of zonal mean vertical velocity (Pa/s; in shaded colors) in the
 24 latitude pressure plane with overlaid zonal mean wind vectors (v ; $-100 \cdot \omega$) [m/s; $100 \cdot \text{Pa/s}$]
 25 anomaly response following strong El Niño and La Niña forcing in winter (DJF) season. The length
 26 and direction of arrows depict the intensity (m/s) and direction of air movement in the latitude
 27 pressure plane respectively.

28 **Figure 5:** Composited mean meridional-mean (20S-20N) anomaly of vertical velocity (Pa/s) in the
 29 longitude pressure plane with overlaid meridional averaged (20°S-20°N) wind vectors (u ; $-$
 30 $1000 \cdot \omega$) [m/s; $1000 \cdot \text{Pa/s}$] anomaly response in HiRAM (left panel) and CFSR (right panel)
 31 following strong El Niño and La Niña forcing in winter (DJF) season. The length and direction of
 32 arrows depict the intensity (m/s) and direction of air movement in the longitude pressure plane.

33 **Figure 6:** Composited mean geopotential height anomaly at 850-hPa following strong El Niño and
 34 La Niña forcing in winter (DJF) season.

35 **Figure 7:** Composited mean geopotential height anomaly at 200-hPa following strong El Niño and
 36 La Niña forcing in winter (DJF) season.

1 **Figure 8:** Composited mean 2m surface temperature anomaly pattern following weak El Niño and
2 La Niña forcing in winter (DJF) season.

3 **Figure 9:** Composited mean precipitation (mm/d) anomaly following weak El Niño and La Niña
4 forcing in winter (DJF) season.

5 **Figure 10:** Composited mean anomaly of zonal mean vertical velocity (Pa/s; in shaded colors) in
6 the latitude pressure plane with overlaid zonal mean wind vectors (v ; $-100 \cdot \omega$) [m/s; $100 \cdot \text{Pa/s}$]
7 anomaly response following weak El Niño and La Niña forcing in winter (DJF) season. The length
8 and direction of arrows depict the intensity (m/s) and direction of air movement in the latitude
9 pressure plane respectively.

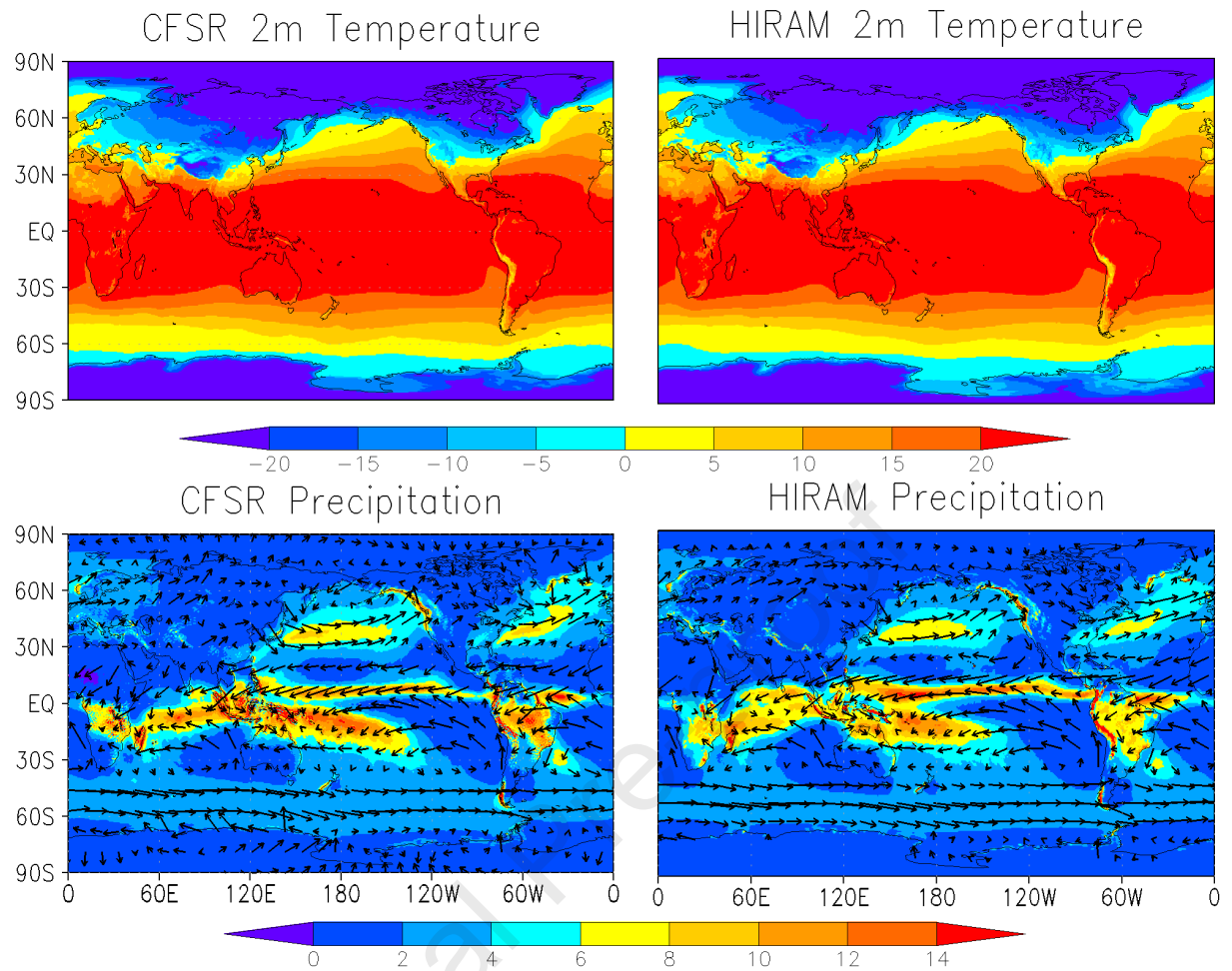
10 **Figure 11:** Composited mean meridional-mean (20°S - 20°N) anomaly of vertical velocity (Pa/s) in
11 the longitude pressure plane with overlaid meridional averaged (20°S - 20°N) wind vectors (u ; $-$
12 $1000 \cdot \omega$) [m/s; $1000 \cdot \text{Pa/s}$] anomaly response following weak El Niño and La Niña forcing in
13 winter (DJF) season. The length and direction of arrows depict the intensity (m/s) and direction of
14 air movement in the longitude pressure plane.

15 **Figure 12:** Composited mean geopotential height anomaly at 850-hPa following weak El Niño and
16 La Niña forcing in winter (DJF) season.

17 **Figure 13:** Composited mean geopotential height anomaly at 200-hPa following weak El Niño and
18 La Niña forcing in winter (DJF) season.

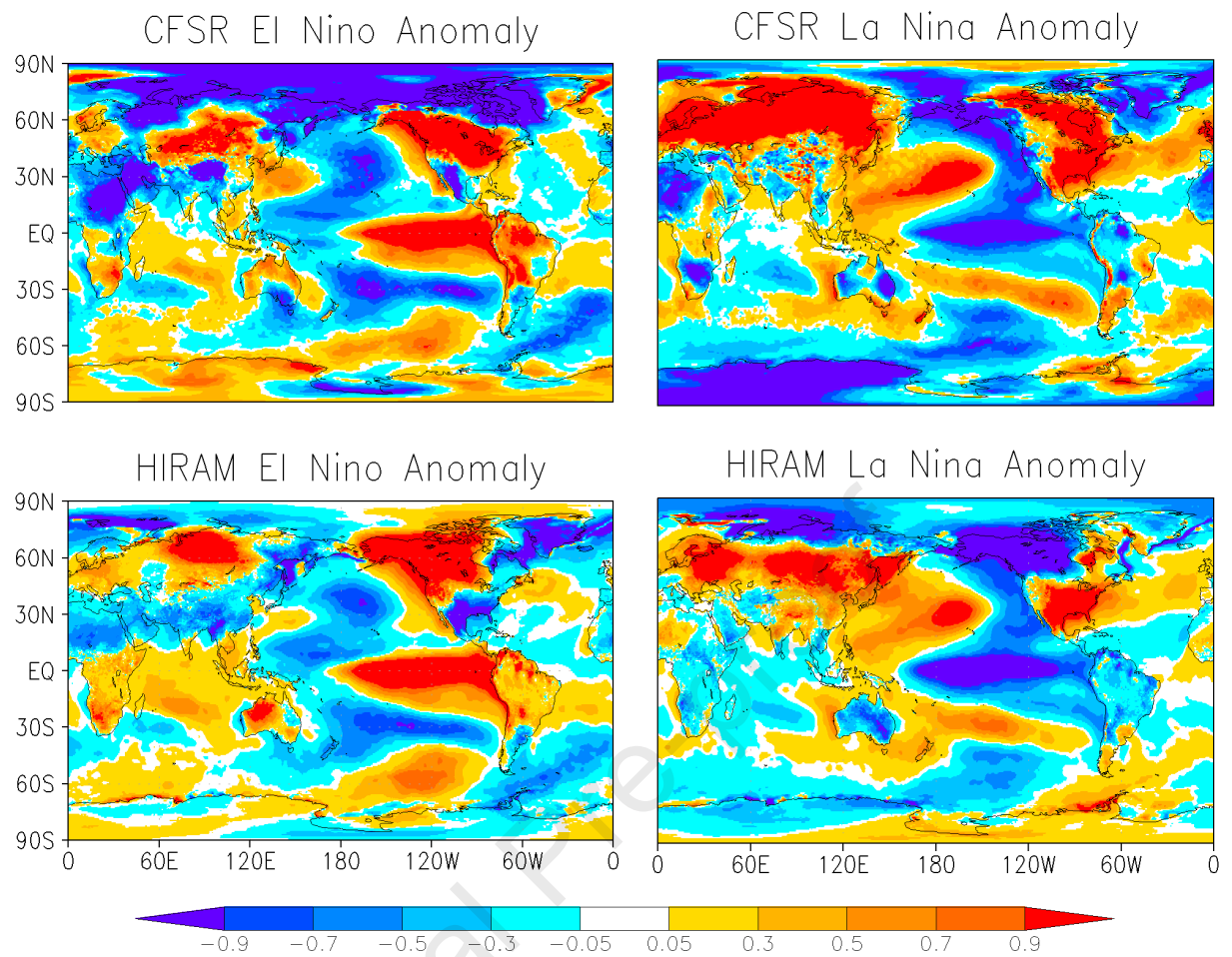
19

20



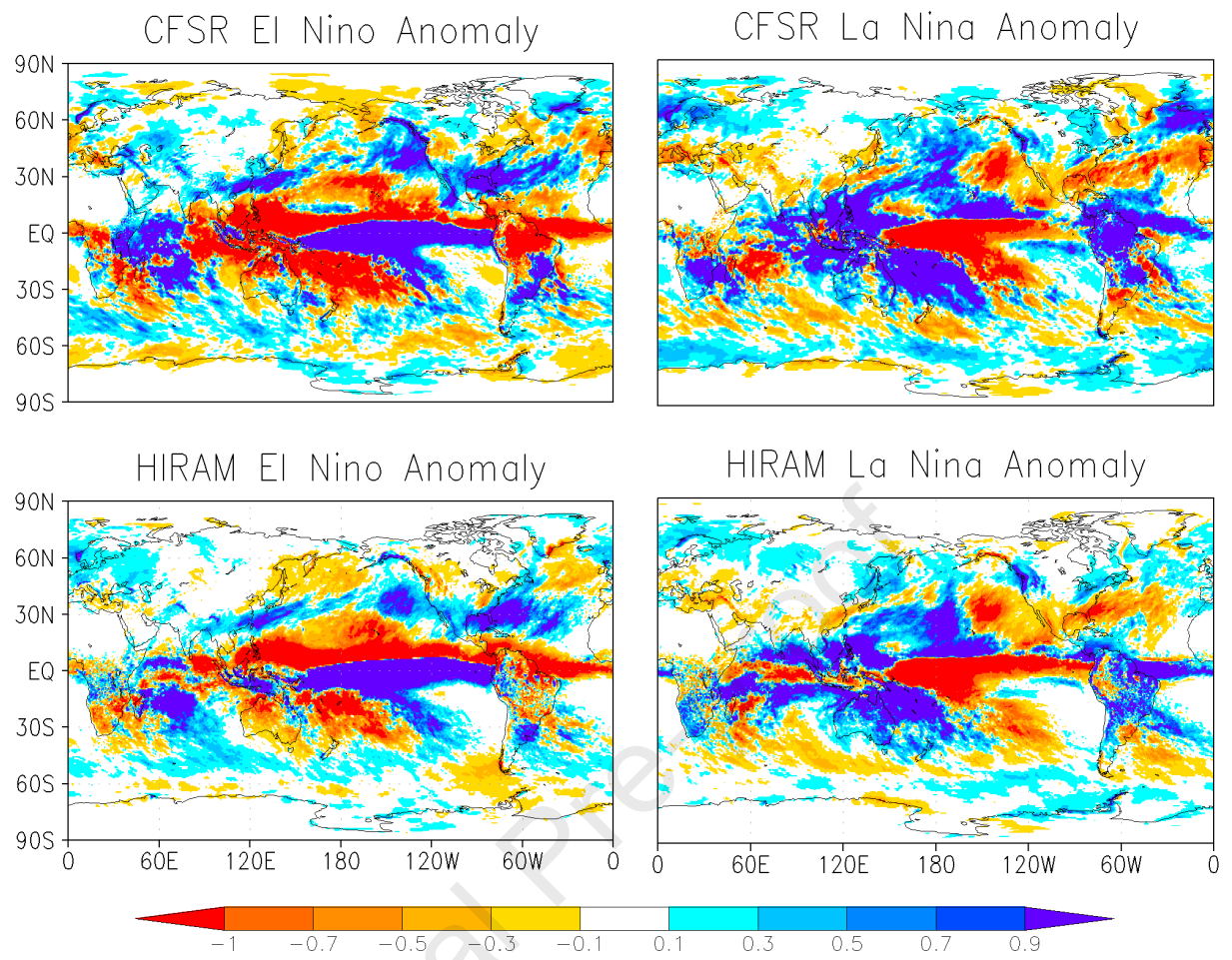
1
2
3
4
5
6

Figure 1: Compositied mean spatial pattern of 2m surface air temperature ($^{\circ}\text{C}$ in top) and precipitation (mm/day in bottom) in winter season produced using CFSR (left panel) and HiRAM simulation (right panel). Wind vectors are also overlaid from CFSR (left bottom panel) and HiRAM (right bottom panel).



1
2
3
4
5

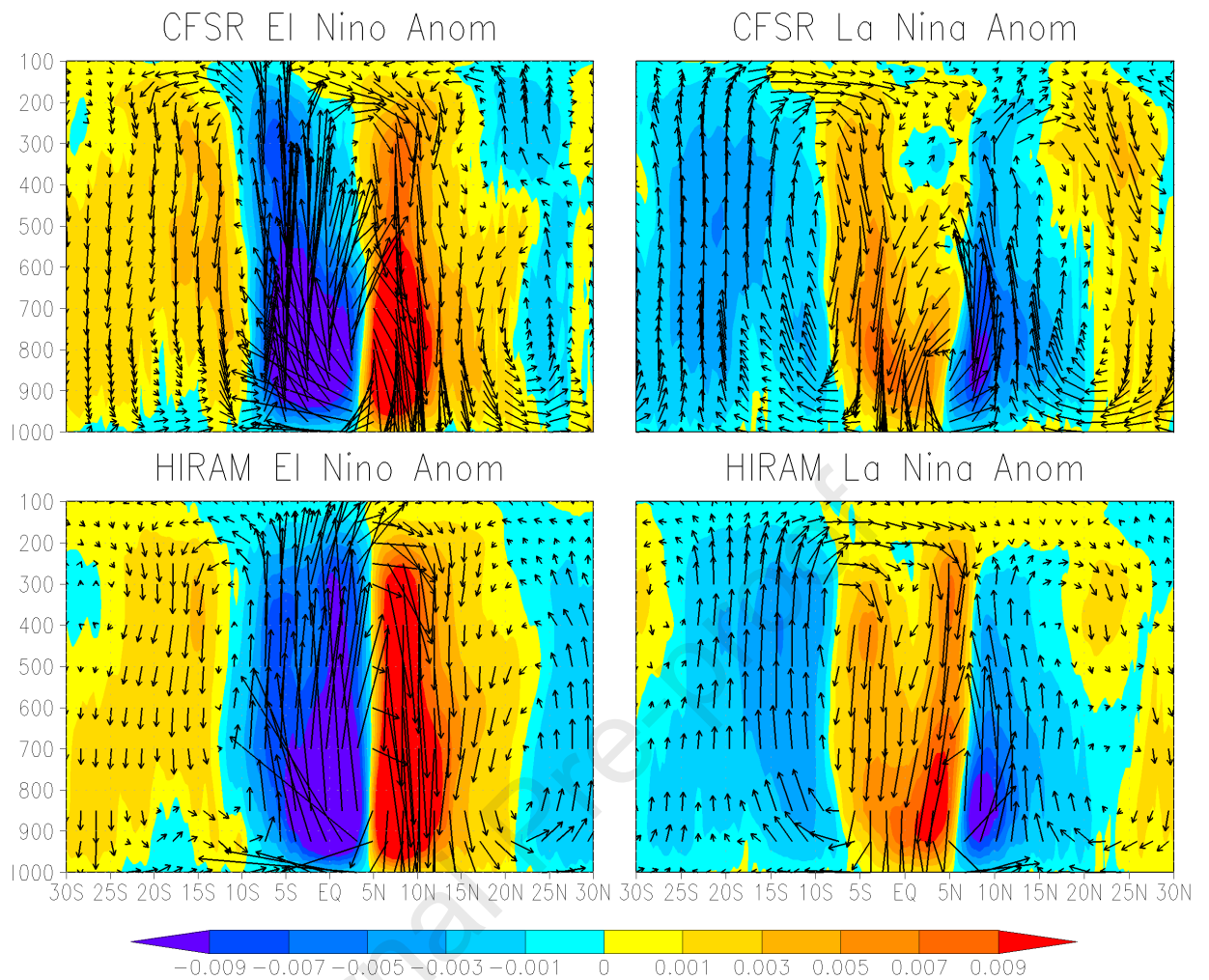
Figure 2: Composited mean 2m surface temperature anomaly pattern from HiRAM (left panel) and CFSR (right panel) following strong El Niño and La Niña forcing in winter (DJF) season.



1

2 **Figure 3:** Composites mean precipitation (mm/d) anomaly from HiRAM (left panel) and CFSR

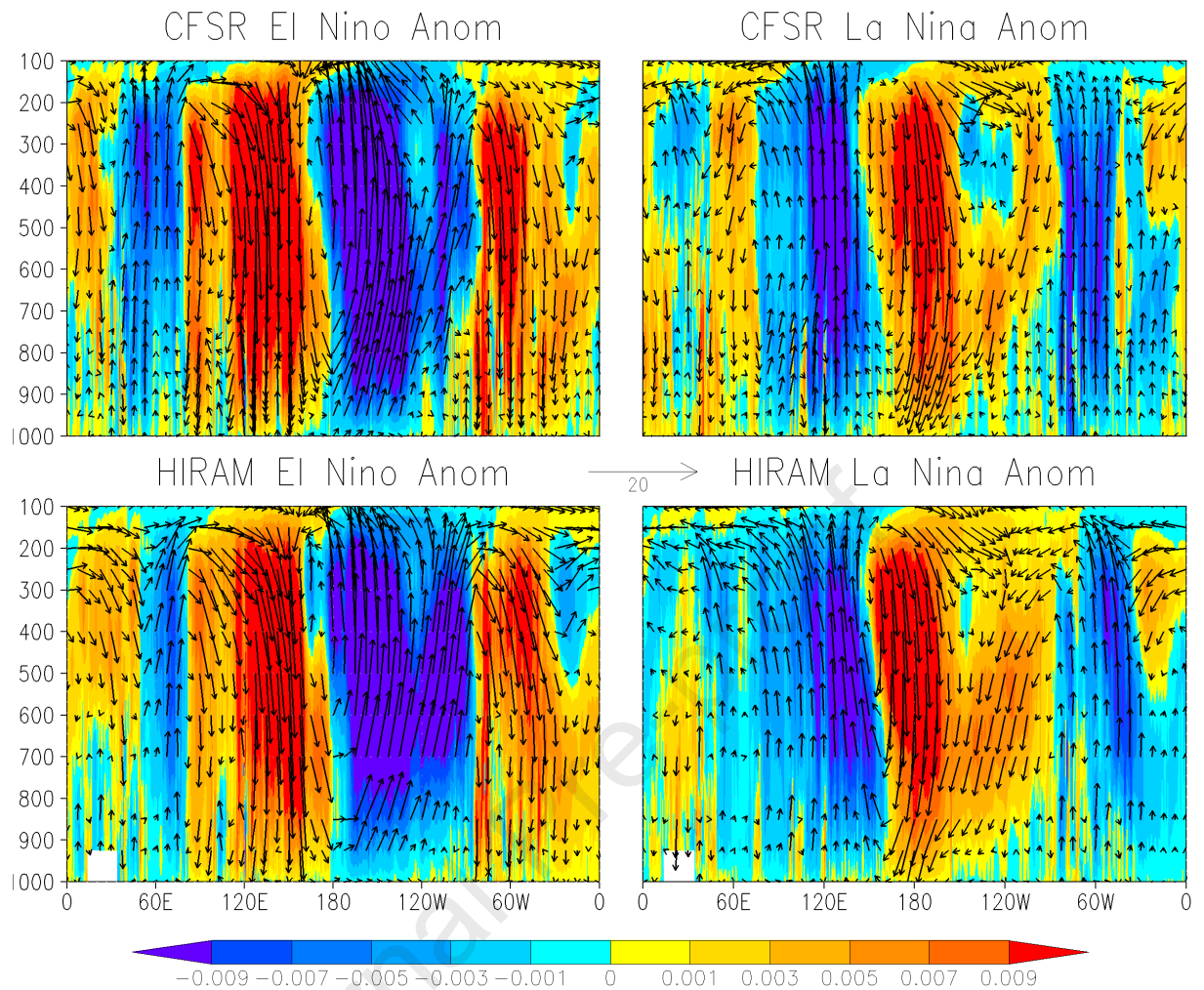
3 (right panel) following strong El Niño and La Niña forcing in winter (DJF) season.



1
2 **Figure 4:** Composited mean anomaly of zonal mean vertical velocity (Pa/s; in shaded colors) in the
3 latitude pressure plane with overlaid zonal mean wind vectors (v ; $-100 \cdot \omega$) [m/s; $100 \cdot \text{Pa/s}$]
4 anomaly response in HiRAM (left panel) and CFSR (right panel) following strong El Niño and La
5 Niña forcing in winter (DJF) season. The length and direction of arrows depict the intensity (m/s)
6 and direction of air movement in the latitude pressure plane respectively.

7

8

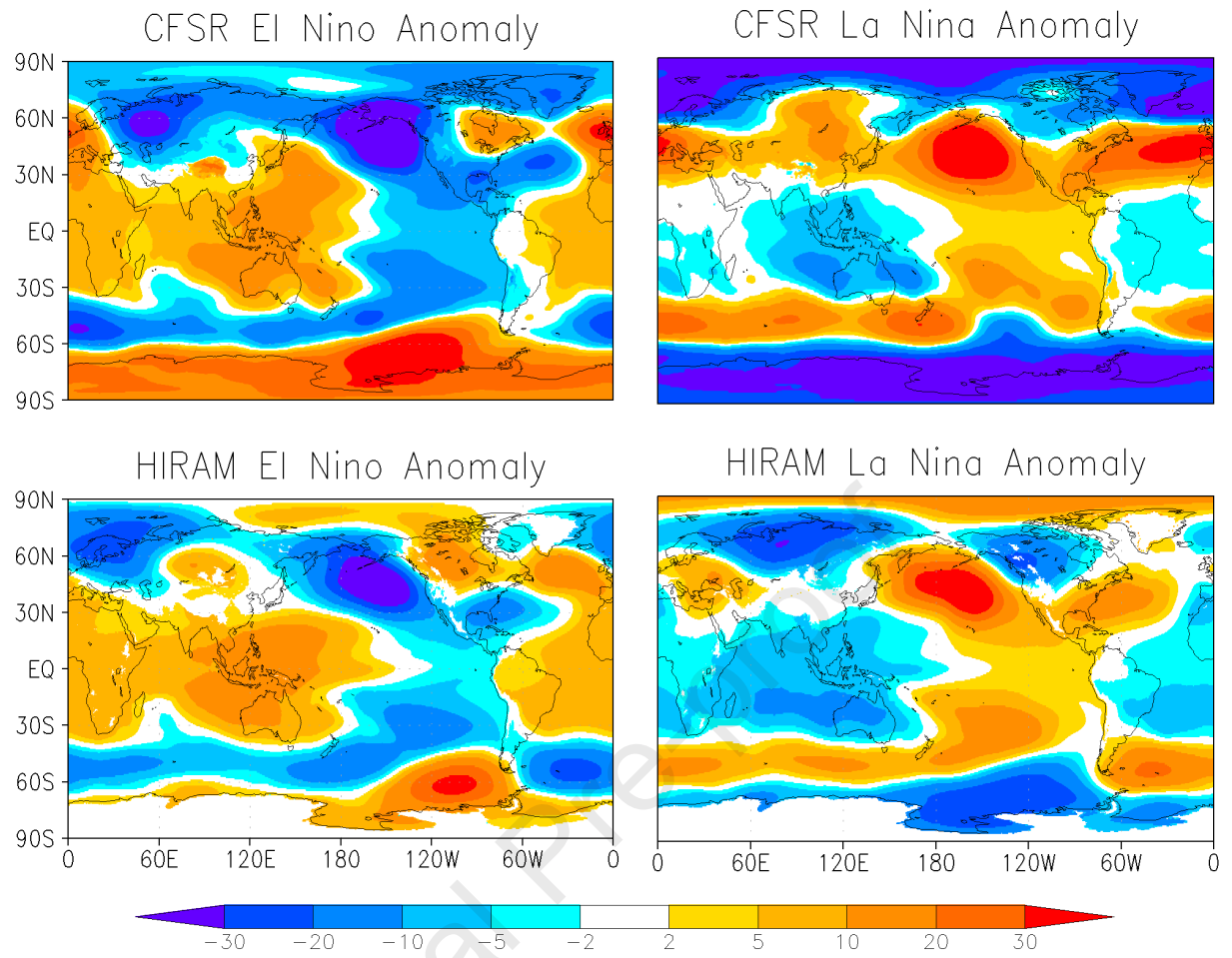


1

2 **Figure 5:** Compositing mean meridional-mean ($20^{\circ}\text{S}-20^{\circ}\text{N}$) anomaly of vertical velocity (Pa/s) in
 3 the longitude pressure plane with overlaid meridional averaged ($20^{\circ}\text{S}-20^{\circ}\text{N}$) wind vectors (u ; $-$
 4 $1000 \cdot \omega$) [m/s; $1000 \cdot \text{Pa/s}$] anomaly response in HiRAM (left panel) and CFSR (right panel)
 5 following strong El Niño and La Niña forcing in winter (DJF) season. The length and direction of
 6 arrows depict the intensity (m/s) and direction of air movement in the longitude pressure plane.

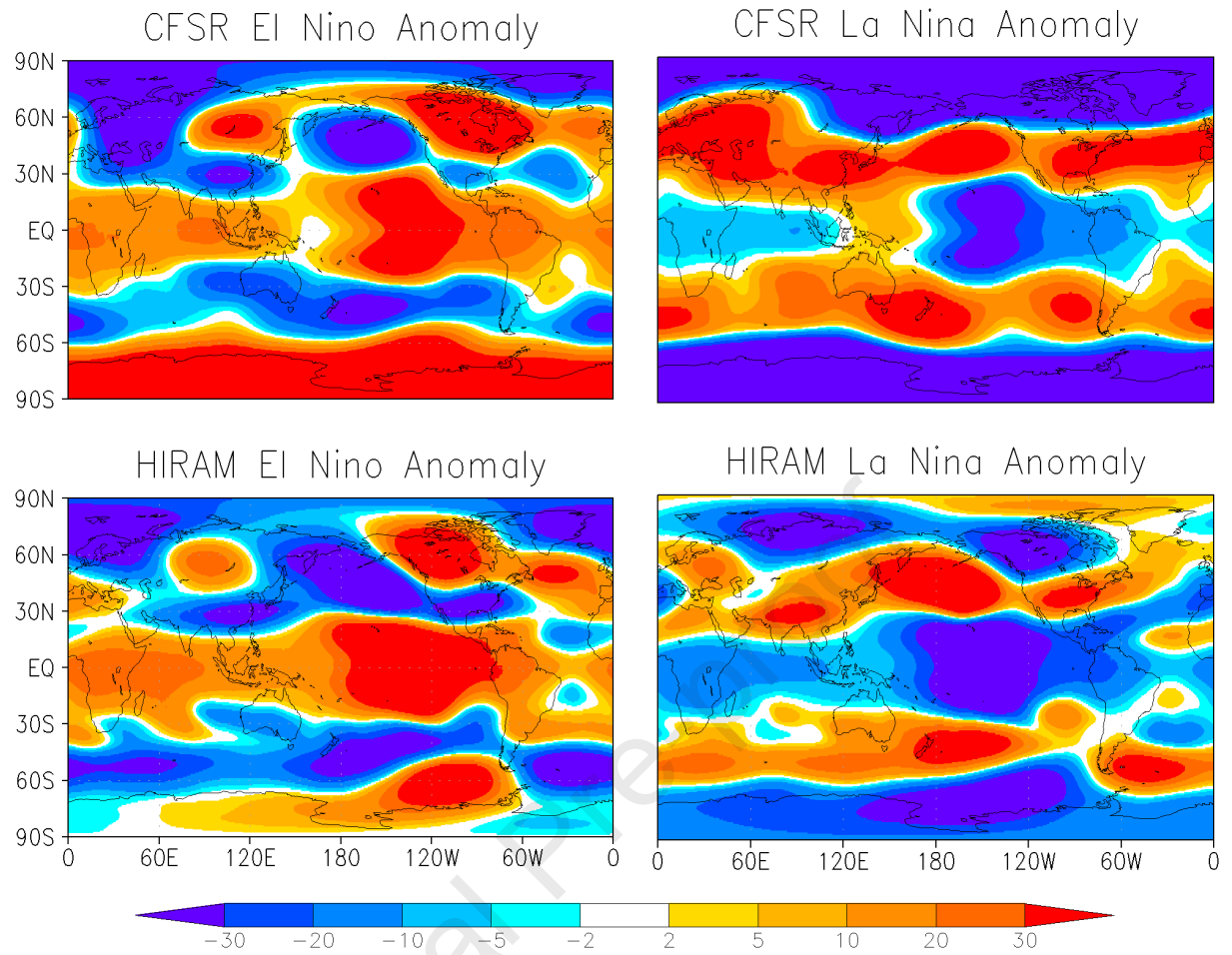
7

8



1
2
3
4
5

Figure 6: Compositing mean geopotential height anomaly at 850-hPa following strong El Niño and La Niña forcing in winter (DJF) season.



1

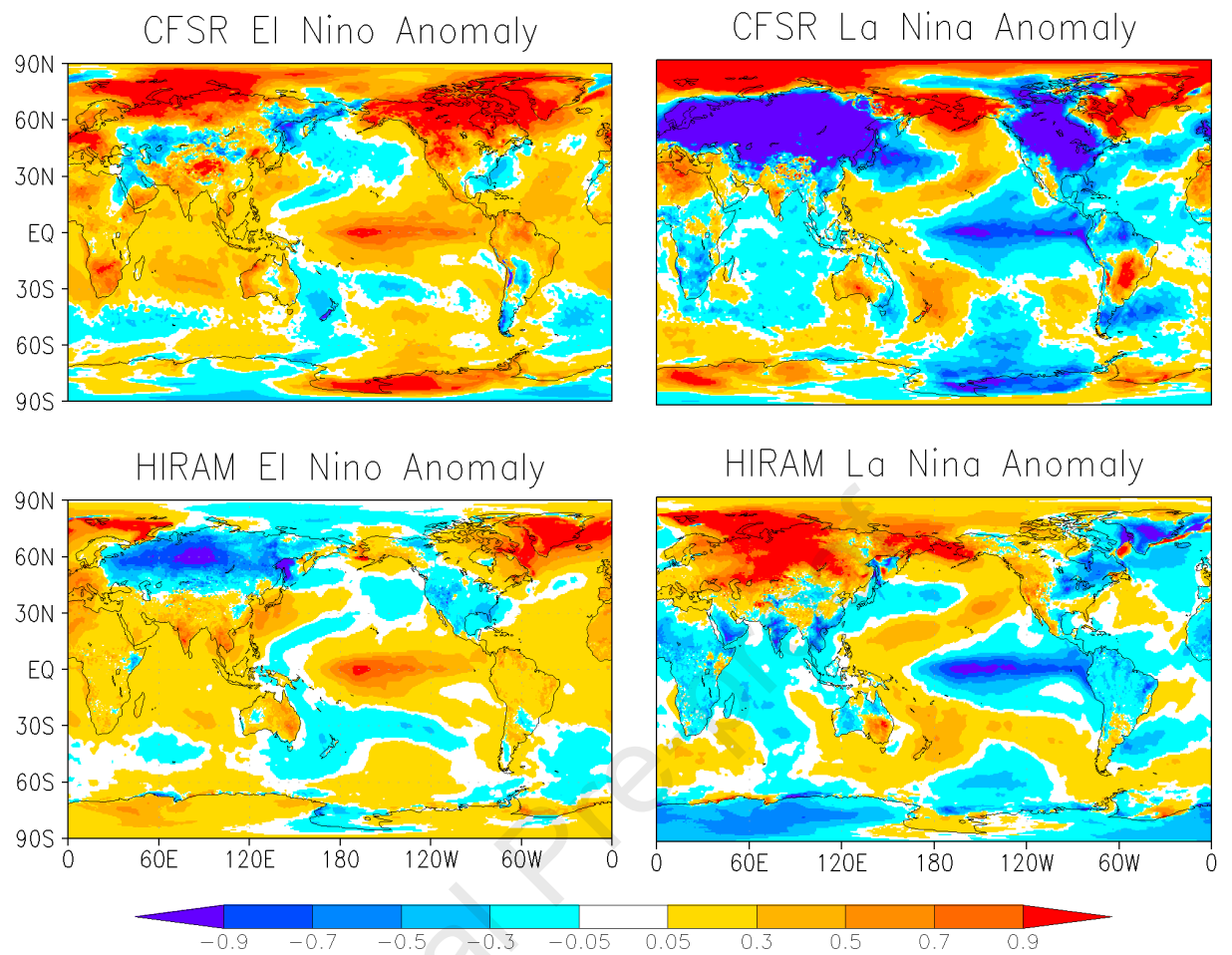
2 **Figure 7:** Composited mean geopotential height anomaly at 200-hPa following strong El Niño and

3 La Niña forcing in winter (DJF) season.

4

5

6

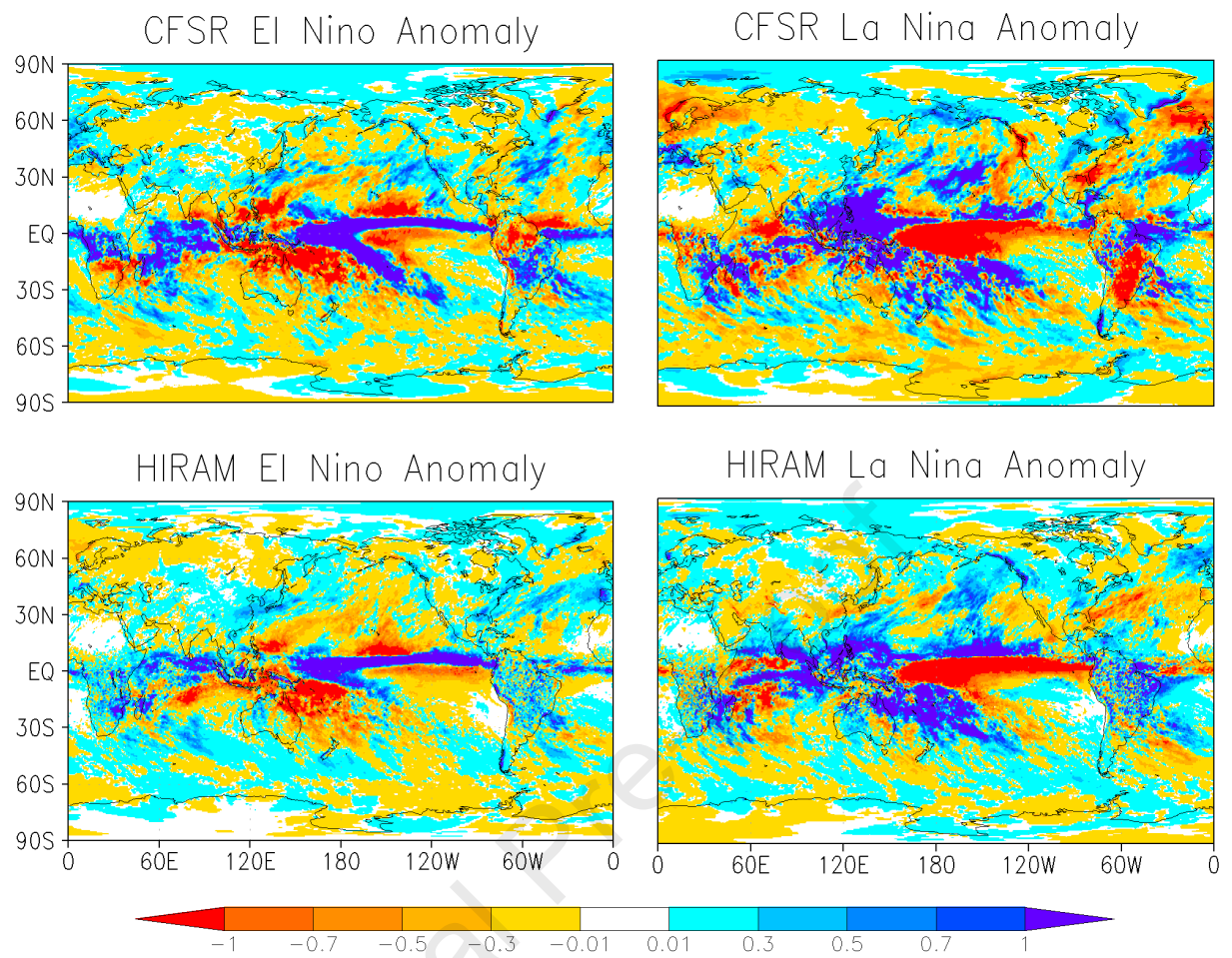


1

2 **Figure 8:** Composited mean 2m surface temperature anomaly pattern following weak El Niño and
3 La Niña forcing in winter (DJF) season.

4

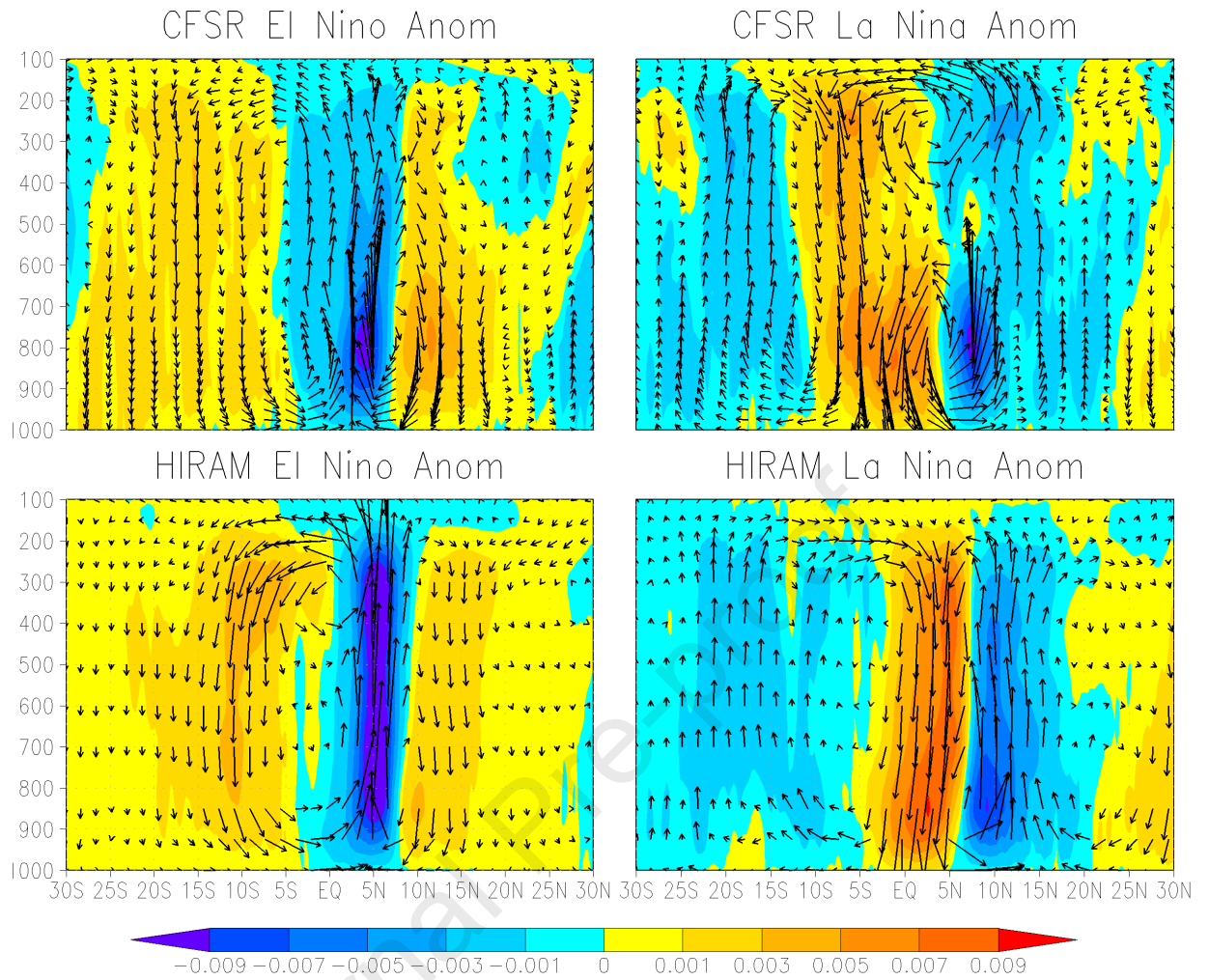
5



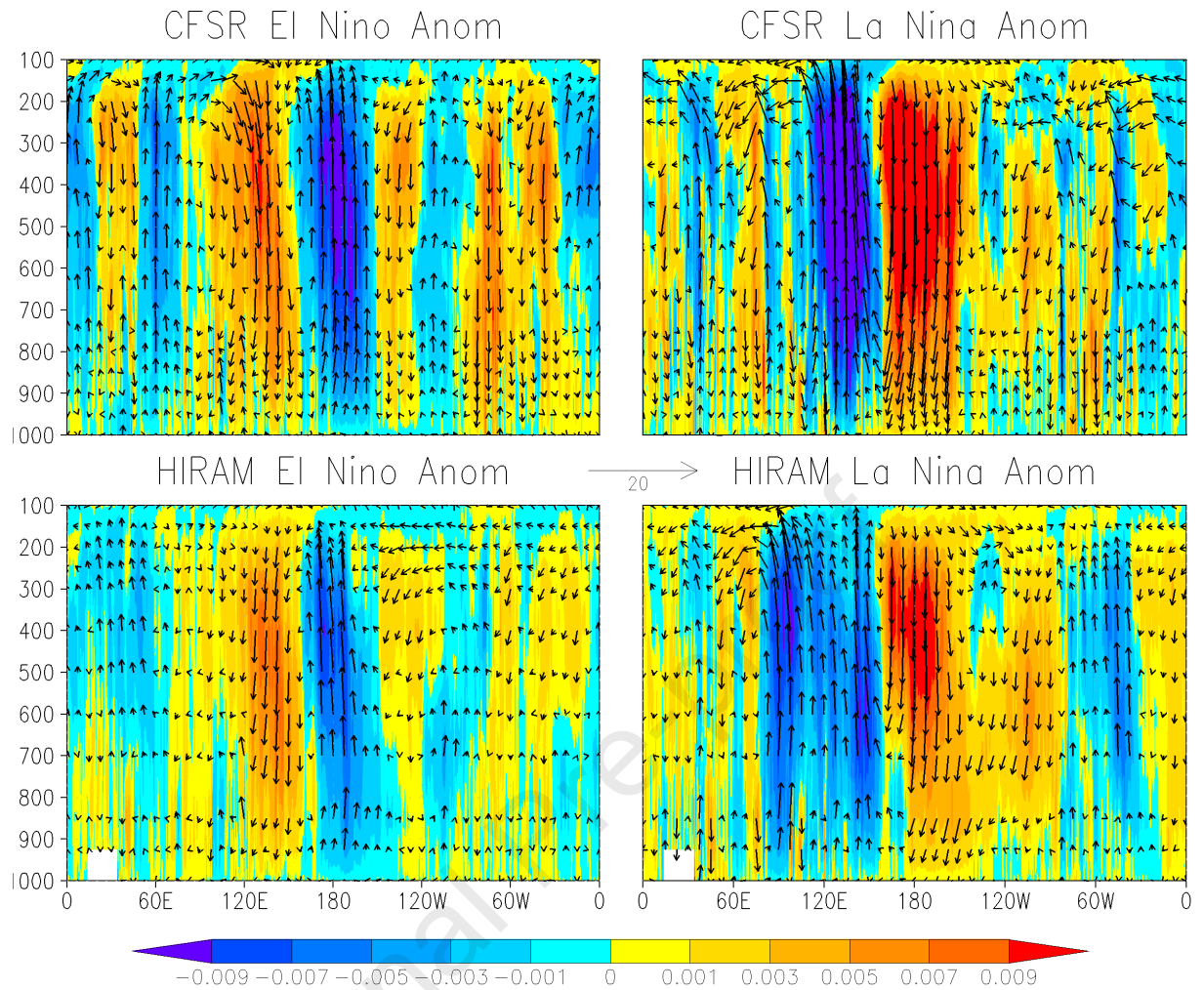
1

2 **Figure 9:** Composites mean precipitation (mm/d) anomaly following weak El Niño and La Niña

3 forcing in winter (DJF) season.



1
 2 **Figure 10:** Composited mean anomaly of zonal mean vertical velocity (Pa/s; in shaded colors) in
 3 the latitude pressure plane with overlaid zonal mean wind vectors (v ; $-100 \cdot \omega$) [m/s; 100*Pa/s]
 4 anomaly response in HiRAM (left panel) and CFSR (right panel) following weak El Niño and La
 5 Niña forcing in winter (DJF) season. The length and direction of arrows depict the intensity (m/s)
 6 and direction of air movement in the latitude pressure plane respectively.



1

2 **Figure 11:** Composites mean meridional-mean (20°S-20°N) anomaly of vertical velocity (Pa/s) in
 3 the longitude pressure plane with overlaid meridional averaged (20°S-20°N) wind vectors (u; -
 4 $100 \cdot \omega$) [m/s; $100 \cdot \text{Pa/s}$] anomaly response in HiRAM (left panel) and CFSR (right panel)
 5 following weak El Niño and La Niña forcing in winter (DJF) season. The length and direction of
 6 arrows depict the intensity (m/s) and direction of air movement in the longitude pressure plane.

7

8

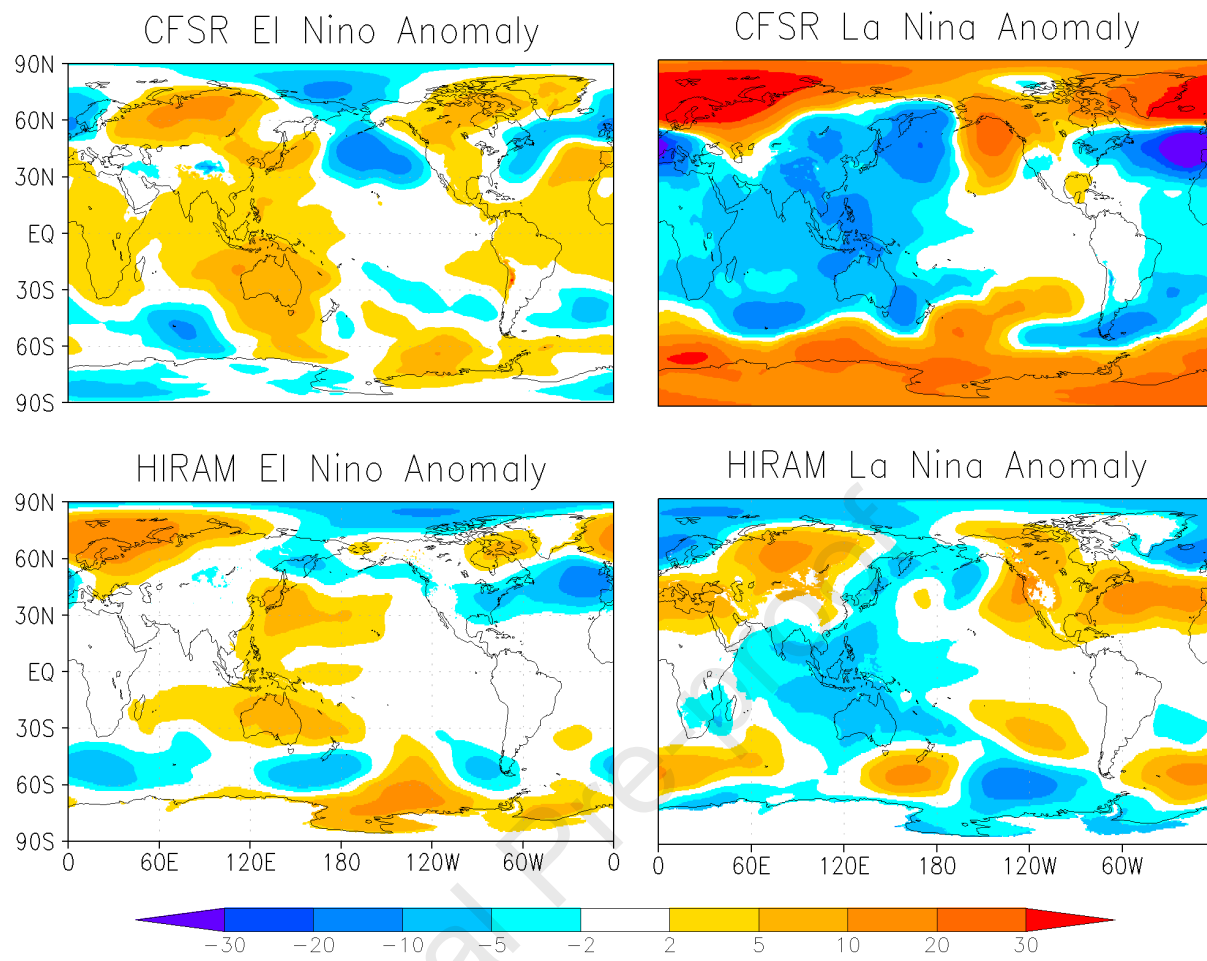
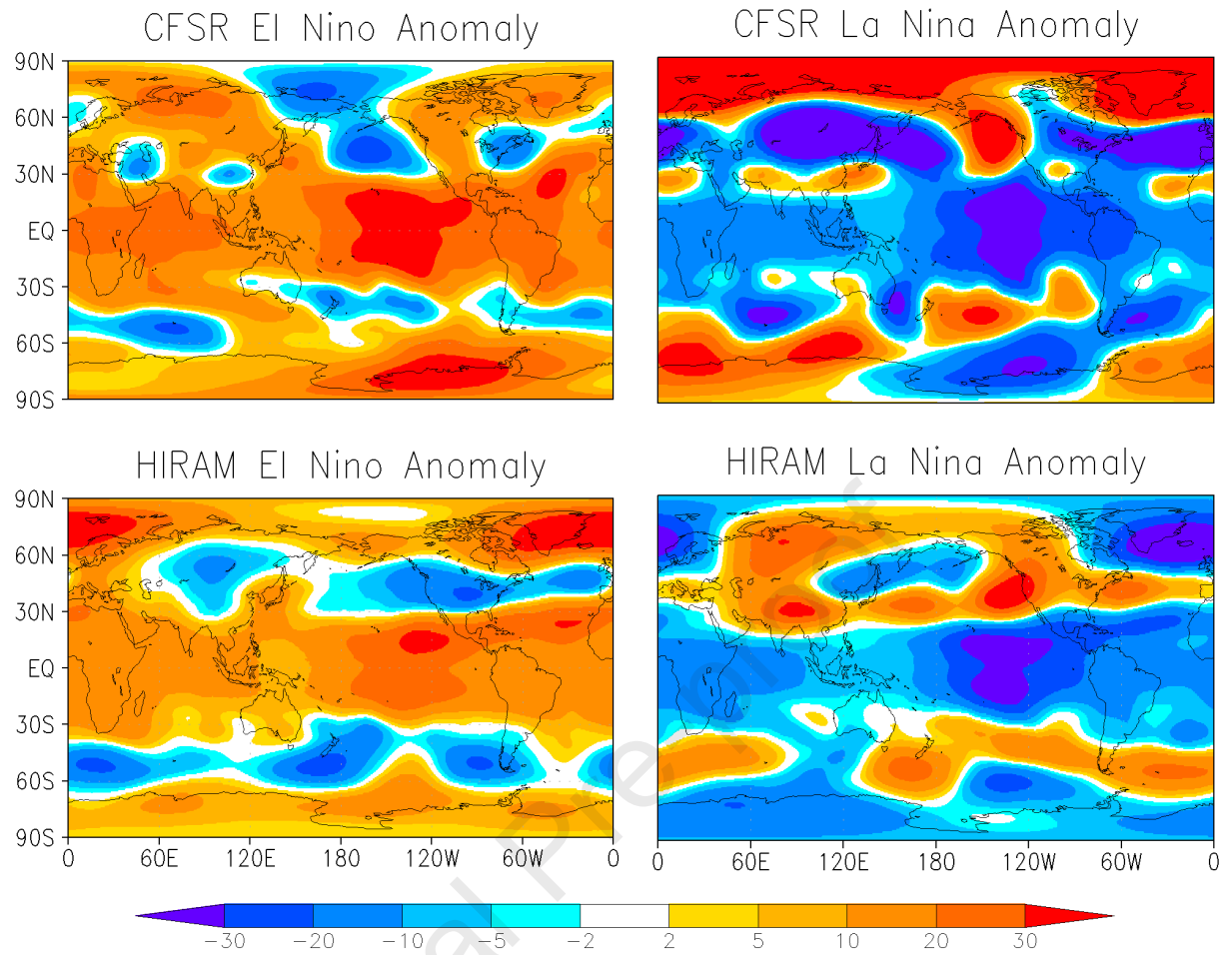


Figure 12: Composites mean geopotential height anomaly at 850-hPa following weak El Niño and La Niña forcing in winter (DJF) season.

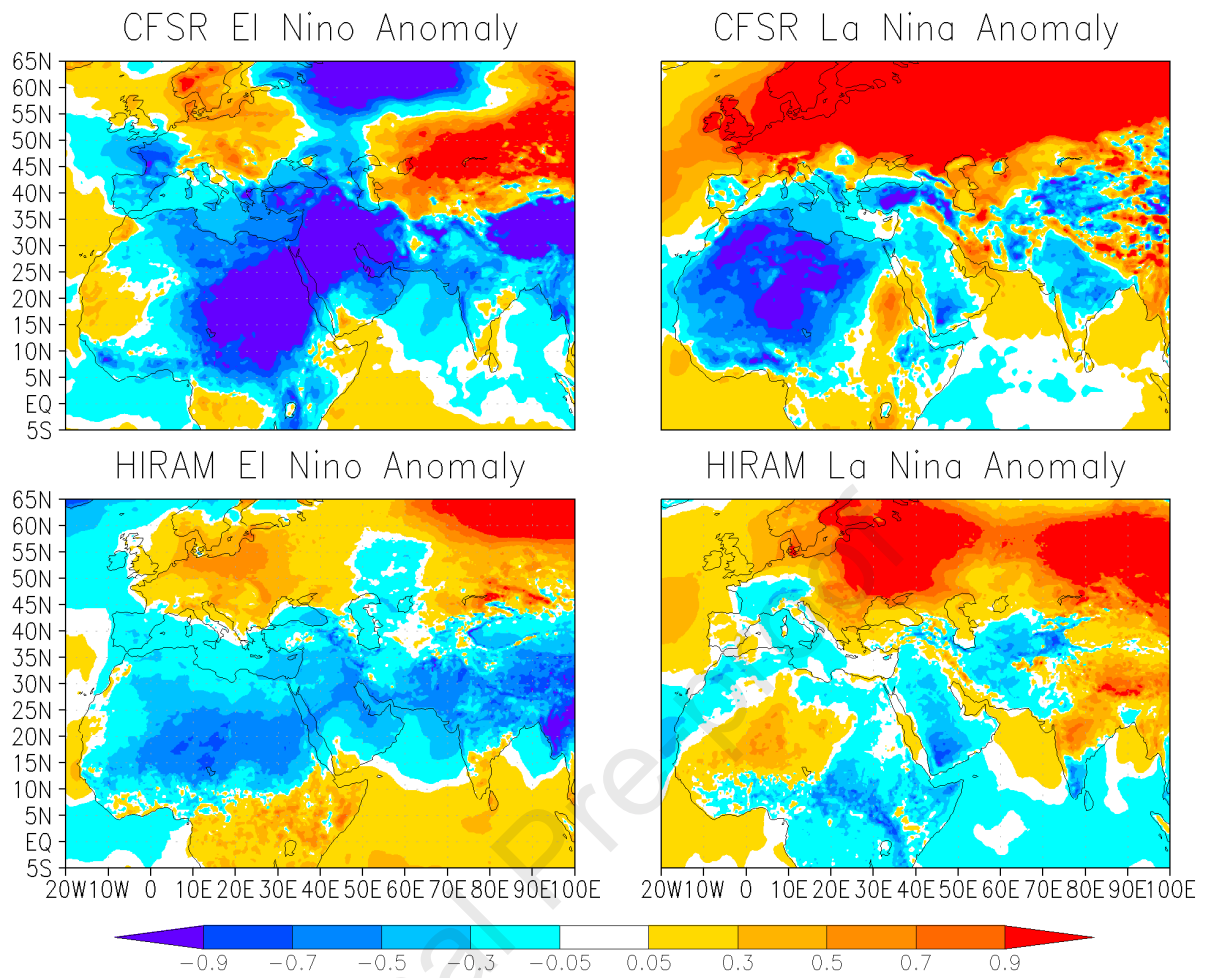
1
2



1

2 **Figure 13:** Composited mean geopotential height anomaly at 200-hPa following weak El Niño and
 3 La Niña forcing in winter (DJF) season.

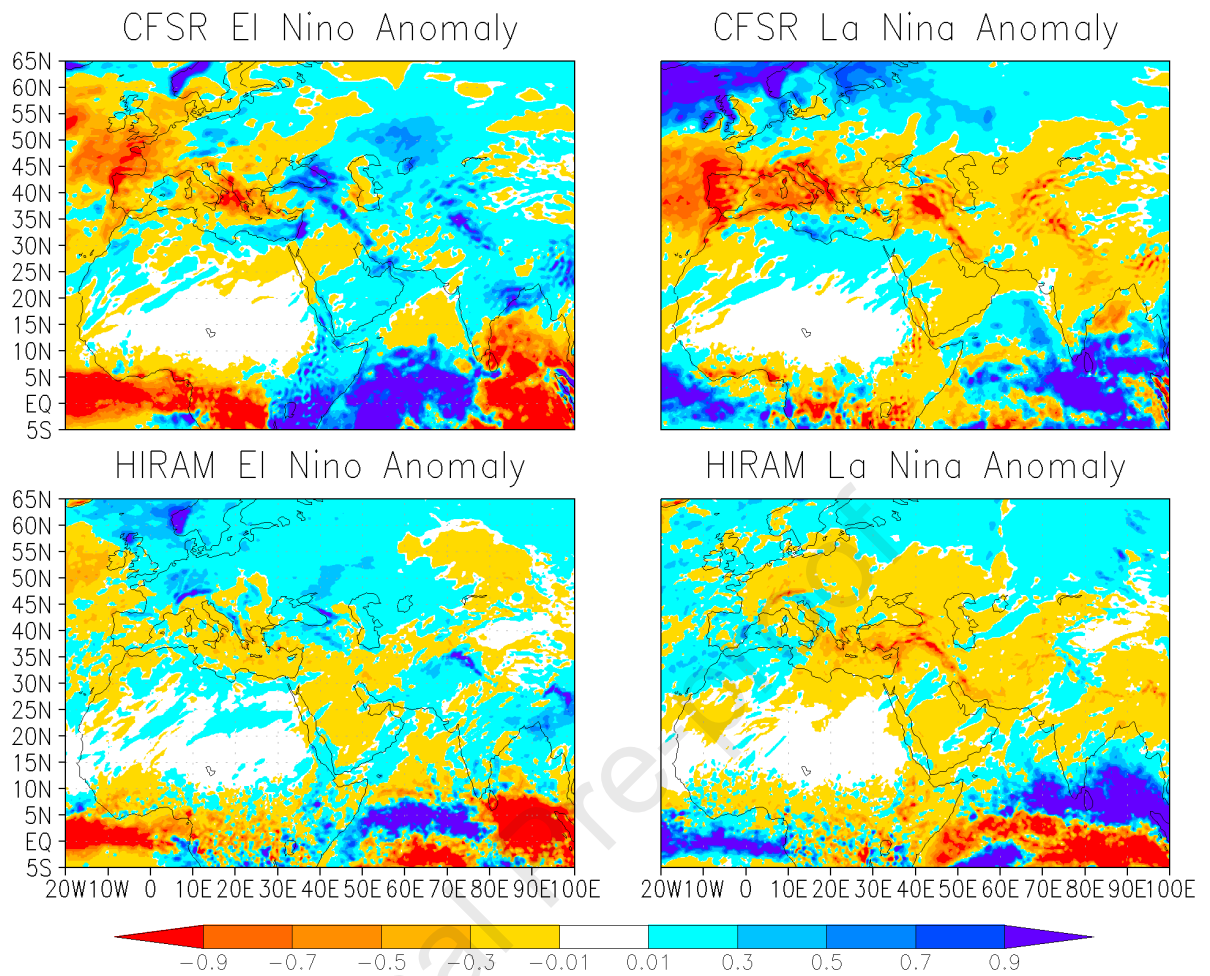
4



1

2 **Figure 14:** Composited mean surface temperature anomaly following strong El Niño and La Niña

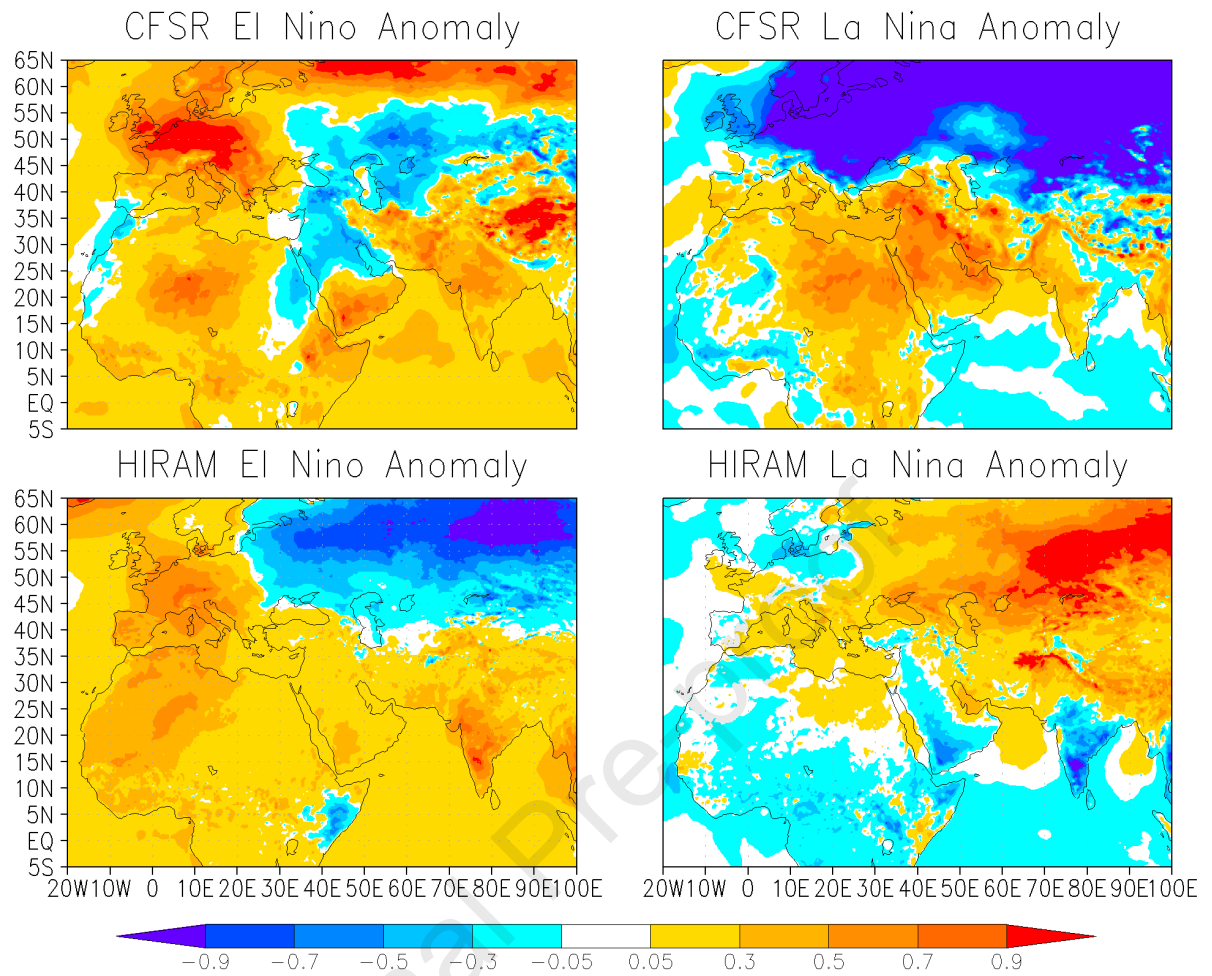
3 forcing over MENA region in winter (DJF) season.



1

2 **Figure 15:** Composites mean precipitation anomaly following strong El Niño and La Niña forcing
 3 over MENA region in winter (DJF) season.

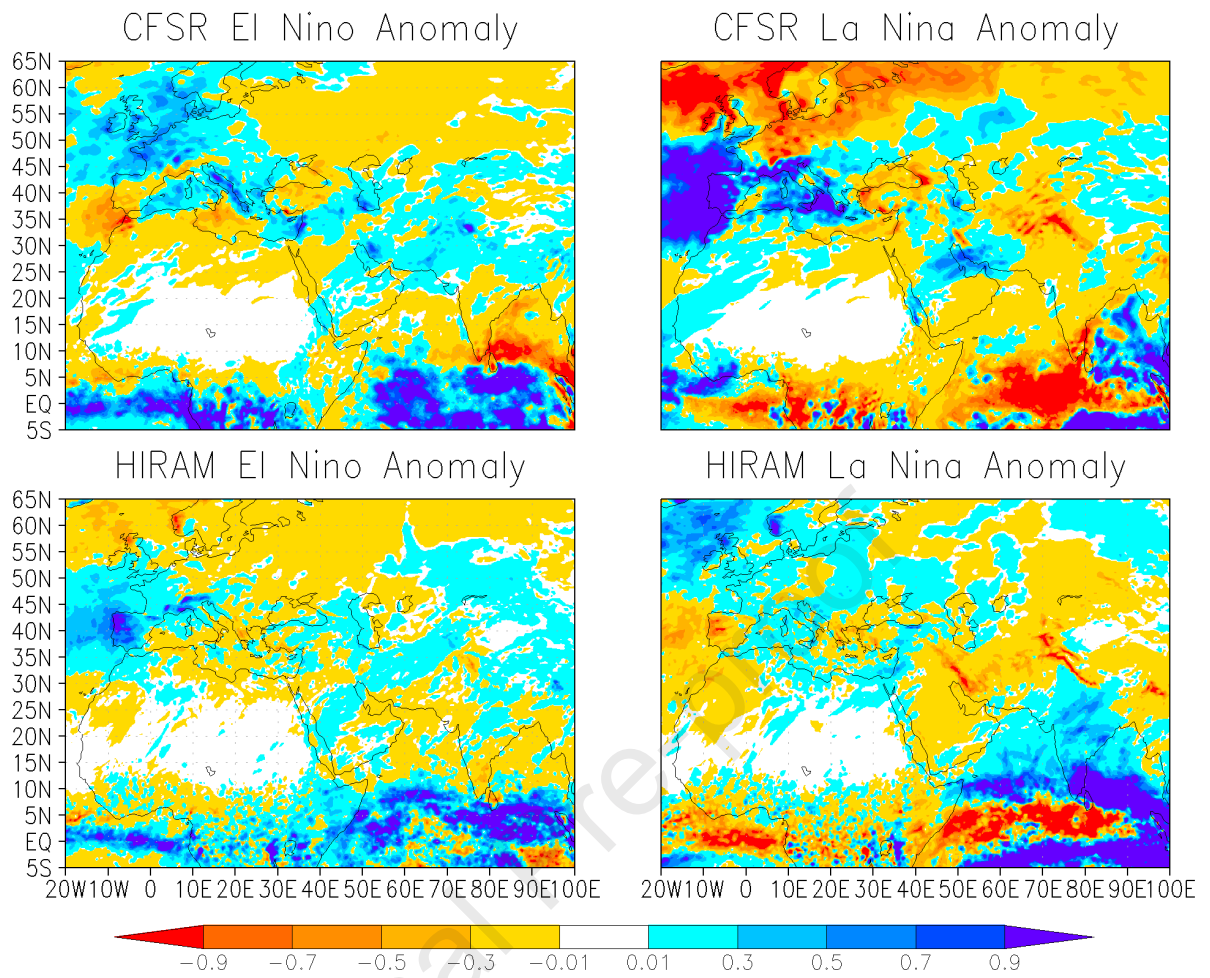
4



1

2 **Figure 16:** Compositing mean surface 2m temperature anomaly following weak El Niño and La
 3 Niña forcing over MENA region in winter (DJF) season.

4



1
 2 **Figure 17:** Composited mean precipitation anomaly following weak El Niño and La Niña forcing
 3 over MENA region in winter (DJF) season.

Highlights

- This research used HiRAM AMIP-style simulations to study the climatic impacts of ENSO strength.
- The strong ENSO initiates a strong PNA (NAO)-like response in the North Pacific (North Atlantic) Ocean.
- MENA & South Asian regions are highly sensitive to ENSO variability & associated teleconnections.
- ENSO impacts are much stronger over ITCZ compared to extratropics & high latitude regions.
- Improved air-sea coupling & model top could reduce the bias between observations & climate model.

Author declaration

1. Conflict of Interest

No conflict of interest exists.

We wish to confirm that there are no known conflicts of interest associated with this publication and there has been no significant financial support for this work that could have influenced its outcome.

2. Funding

No funding was received for this work.

3. Intellectual Property

We confirm that we have given due consideration to the protection of intellectual property associated with this work and that there are no impediments to publication, including the timing of publication, with respect to intellectual property. In so doing we confirm that we have followed the regulations of our institutions concerning intellectual property.

4. Research Ethics

We further confirm that any aspect of the work covered in this manuscript that has involved human patients has been conducted with the ethical approval of all relevant bodies and that such approvals are acknowledged within the manuscript.

5. Authorship

All listed authors meet the Journal criteria. We attest that all authors contributed significantly to the creation of this manuscript, each having fulfilled criteria as established by the journal.

We confirm that the manuscript has been read and approved by all named authors.

We confirm that all named authors have approved the order of authors listed in the manuscript.

6. Contact with the Editorial Office

The Corresponding Author declared on the title page of the manuscript is:

Dr. Muhammad Mubashar Dogar (mubashardogar@yahoo.com)

This author submitted this manuscript using his account in Atmospheric Environment.

We understand that this Corresponding Author is the sole contact for the Editorial process and direct communications with the office. He is responsible for

communicating with the other authors about progress, submissions of revisions and final approval of proofs.

We confirm that the email address shown below is accessible by the Corresponding Author, is the address to which Corresponding Author's EVISE account is linked, and has been configured to accept email from the editorial office of Atmospheric Environment.

mubashardogar@yahoo.com

The undersigned agree with all of the above.

Dr. Muhammad Mubashar Dogar

Journal Pre-proof